

# Effect of machine stiffness on interpreting contact force-indentation depth curves in adhesive elastic contact experiments

Weilin Deng<sup>a</sup>, Haneesh Kesari<sup>a,\*</sup>

<sup>a</sup>*School of Engineering, Brown University, Providence, RI 02912*

---

## Abstract

Dry adhesion plays a critical role in many fields, including the locomotion of some insects and failure of microelectromechanical systems. The Dupré's work of adhesion of a contact interface is an important metric of dry adhesion. It is often measured by applying the Johnson-Kendall-Roberts (JKR) theory [1] to contact force-indentation depth curves that are measured using an atomic force microscope (AFM), or an instrument modeled after it. The JKR theory has been exceptionally successful in interpreting contact force-indentation depth measurements and explaining adhesive, elastic contact phenomena, such as the pull-in and pull-off instabilities. However, in many cases the JKR theory predicts a lower magnitude for the pull-off force than what is experimentally measured, and it does not capture the finite changes in the indentation depth that occur during the pull-in and pull-off instabilities. In those cases, applying the JKR theory to calculate the work of adhesion from only the measured pull-off force is likely to give highly inaccurate results. We believe that these discrepancies occur because the classical JKR theory ignores the machine stiffness—which, in the case of AFM-type instruments, is the stiffness of the mechanical structure that connects the tip to the translation stage, which moves the tip towards and away from the substrate. In this paper, we present a model that is related to, but more general than, the JKR theory that accounts for the machine stiffness. This model explains the experimental data better than the JKR theory in the cases where the JKR theory displays the aforementioned discrepancies. We consider both the first order necessary and the higher order sufficiency conditions while deriving the solutions in our model.

*Keywords:* Adhesion, Contact experiment, Machine stiffness, JKR, Pull-in instability, Pull-off instability, Hysteretic energy loss

*PACS:* 68.35.Np, 46.55.+d

---

\*Corresponding author

*Email address:* haneesh\_kesari@brown.edu (Haneesh Kesari)

## 1. Introduction

Van der Waals (dipole-dipole) and Coulombic interactions between molecules can give rise to attractive forces between solids [2, 3]. These attractive forces can make a pair of contacting surfaces adhesive even when they are not connected by any liquid bridges. The effect of these attractive forces, termed *dry adhesion*, operates at all scales but is dominant at  $\mu\text{m}$ – $\text{nm}$  lengths (Figure 1a).

Dry adhesion has been found to play an important role in many fields, including biology, engineering, and physics. Many insects, spiders, and reptiles, for example, possess fibrillar structures on their foot pads that, through adhesion, allow these animals to adeptly scale vertical surfaces [4–9] (Figure 1b). In microelectromechanical systems (MEMS) engineering, adhesion-induced device failure is a pervasive problem that limits its continued development. In MEMS devices, such as comb drive accelerometers, slender, micrometer-sized structures are aligned in parallel rows in close proximity to one another (Figure 1c). During the device’s fabrication stage or later in its operation, these structures can unintentionally come into contact with each other or the substrate and remain permanently adhered, leading to device failure [10]. Adhesion also plays a role in the physical properties that underlie friction and wear at the sub-micrometer scale [11, 12]. Contact between hard solids, such as metals and ceramics, primarily takes place at the surfaces’ asperities. Adhesion firmly welds the asperities, and thus the two solids. In order to move or slide the solids over one another, significant frictional force must be generated in order to break the asperities apart or rupture the asperities from their respective solids, contributing to wear (Figure 1d).

An important metric for quantifying dry adhesion between two contacting solids is the Dupré’s work of adhesion,

$$w := \gamma_1 + \gamma_2 - \gamma_{12}, \quad (1.1)$$

where  $\gamma_1$  and  $\gamma_2$  are the surface energies of the two solids and  $\gamma_{12}$  is the contact interface’s energy per unit area [14]. Adhesion can be measured through a variety of tests and experiments, including thin film peeling [15–17], blister tests [18, 19], and normal contact experiments [20–27]. Among these techniques, normal contact experiments distinguish themselves for two reasons: firstly, they can provide information about the materials’ elastic properties; and secondly, they can spatially map out a material’s surface adhesive and bulk elastic properties at the  $\mu\text{m}$ – $\text{nm}$  length scales, making it the preferred test for evaluating adhesion and the elasticity of a solid.

Normal contact experiments are typically performed using an atomic force microscope (AFM) [20–24] or an instrument modeled after it. In these experiments, a sample of the material whose properties are to be examined is prepared in the form of a rectangular or circular slab. This slab is most commonly referred to as the substrate. The substrate is placed under a rigid tip, which is connected to a stage via a passive mechanical structure, such as the cantilever in an AFM (Figure 2a). The instrument controls the position of the stage and brings the tip and substrate into and out of contact. Mechanical properties are

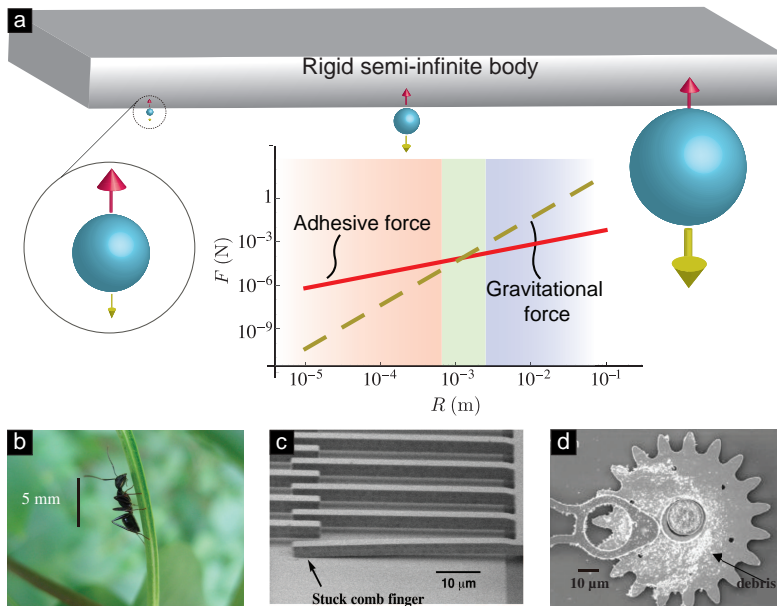


Figure 1: (a) Adhesion dominates at small scales. Bradley [13] considered the adhesive force between a rigid sphere and a rigid semi-infinite body. He assumed that the adhesive interaction between two molecules of the solids, with centers a distance  $d$  apart, is proportional to  $1/d^n$  where  $n$  is an integer. The adhesive force is found to be  $2\pi wR$ , where  $w$  is the work of adhesion and  $R$  is the radius of the sphere. At the same time, the gravitational force on the sphere is  $4\pi\rho gR^3/3$  where  $\rho$  is the density of the material of which the sphere is composed. For most engineering materials,  $w$  and  $\rho$  are of the order of  $10 \text{ mJ/m}^2$  [14] and  $10^3 \text{ kg/m}^3$ , respectively. (b) An ant climbs on a plant stem, showcasing that adhesive forces overcome the gravitational forces at small length scales. (c) A comb finger of a drive actuator is stuck to the substrate due to adhesion [10]. (d) Wear debris accumulates on the surface of the gear of a microengine [10] as a result of adhesion.

44 measured at a given location on a substrate’s surface by carrying out one or  
 45 more contact cycles. Each contact cycle begins with a loading phase, when the  
 46 stage moves towards the substrate, followed by an unloading phase, when the  
 47 stage moves away from the substrate. During contact cycles, the deformation  
 48 of the mechanical structure that connects the stage to the tip is often small,  
 49 resembling an elastic spring. The stiffness of this spring is referred to as the  
 50 *machine stiffness*. In AFM contact experiments, the mechanical structure that  
 51 connects the tip to the stage is a cantilever. The cantilever’s shape, size, and  
 52 material composition then dictate the machine stiffness.

53 In the experiments, the contact force that arises between the two solids is  
 54 measured as a function of the indentation depth which is the distance from the  
 55 undeformed substrate’s surface to the tip. The properties of the substrate are  
 56 obtained from the contact force–indentation depth data based on a classical  
 57 adhesive contact theory such as the Johnson-Kendall-Roberts (JKR) theory [1].  
 58 According to the JKR theory, the tip would jump into contact with the substrate

59 unstably in the loading phase, resulting in an abrupt decrease in the contact  
 60 force. Similarly, in the unloading phase, the tip would jump out of contact with  
 61 the substrate spontaneously, resulting in a sudden increase in contact force.  
 62 The phenomena of the tip jumping into and out of contact with the substrate  
 63 unstably are called *pull-in* and *pull-off* instabilities, respectively. There are two  
 64 important experimental results that differ from the JKR predictions. First, the  
 65 indentation depth just before and after the pull-in and pull-off instabilities do  
 66 not change as per the JKR theory, see Figure 2b. However, in many adhesive  
 67 contact experiments the indentation depth just before and after the pull-in and  
 68 pull-off instabilities are different [20–22, 24], see Figure 2c. Second, the JKR  
 69 theory predicts the contact force at the pull-off instability, i.e. the pull-off force,  
 70 to be  $-5\pi wR/6$ , where  $R$  is the radius of curvature of the tip; whereas the  
 71 measured pull-off force in experiments is different from that value (see §4). The  
 72 work of adhesion would be inaccurate if it were calculated using the pull-off force  
 73 given by the JKR theory. The reason for this difference is due to the machine  
 74 stiffness, whose effect is overlooked in the JKR theory.

75 In this paper, we show that machine stiffness is an important factor in adhe-  
 76 sive contact. Our problem is a model for a class of contact experiments that are  
 77 conducted using an AFM-type instrument. We consider an axisymmetric me-  
 78 chanics problem involving the adhesive, frictionless contact between two solids  
 79 to study the effect of machine stiffness. Both the tip’s symmetry axis and the  
 80 stage’s translational directions are normal to the substrate’s surface that faces  
 81 the tip. We assume that the contact region is simply connected and hence is a  
 82 disk that has its center on the tip’s symmetry axis. Just as in the JKR model [1],  
 83 adhesion in our problem is modeled as an infinitesimal interaction—albeit its  
 84 origins from the van der Waals and Coulombic interactions are finite-ranged.  
 85 More specifically, Johnson *et al.* [1] treated adhesive elastic contact by includ-  
 86 ing an adhesion energy term in the system’s total potential energy, and then  
 87 determined the contact region by stipulating that the contact radius locally  
 88 minimizes the potential energy. We adopt the same methodology as Johnson  
 89 *et al.* [1], and additionally include an elastic energy term that results from the  
 90 deformation of the instrument’s mechanical structure into the total potential  
 91 energy calculation of our model. We use a variational approach in the study  
 92 of our adhesive contact problem and derive the necessary and sufficient condi-  
 93 tions on the solutions to our problem. We remark that Takahashi *et al.* [28]  
 94 and Yang [29] analyzed the effect of machine stiffness on the adhesive contact  
 95 between a paraboloidal tip and an elastic half-space. They too use a variational  
 96 approach. However, our approach is different from that of Takahashi *et al.* and  
 97 Yang in that they only consider the first order necessary conditions on the solu-  
 98 tions to their problems, while in our model we further consider the second order  
 99 sufficiency conditions on the solutions. Second order sufficiency conditions have  
 100 previously been used to study the stability of the equilibrium configurations in  
 101 adhesive elastic contact problems by Kesari and Lew [30], Argatov *et al.* [31],  
 102 Willert *et al.* [32], and Popov *et al.* [33], among others.

103 The outline of the paper is as follows. First, we formulate our contact  
 104 problem using the variational approach and derive the solutions in §2. In §3 we

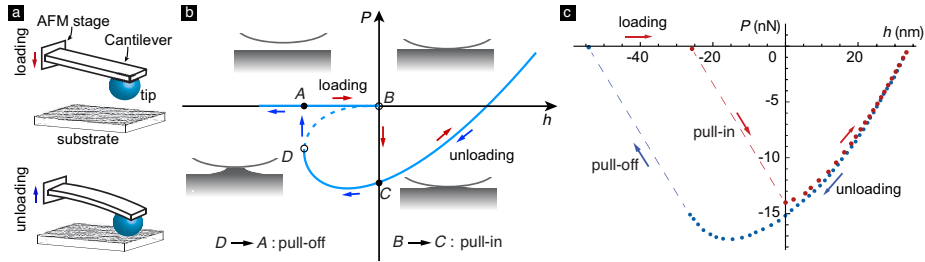


Figure 2: (a) A schematic of an AFM contact experiment. The instrument brings the tip and substrate into and out of contact by controlling the position of the stage, which is connected to the tip by an elastic cantilever. (b) The contact force-indentation depth curve according to the JKR theory. The pull-in instability ( $B \rightarrow C$ ) and pull-off instability ( $D \rightarrow A$ ) are marked along with corresponding contact configurations. (c) The measured contact force-indentation depth data from the contact experiments between a glass bead and a Polydimethylsiloxane (PDMS) substrate [21].

105 consider two tip geometries, spherical and conical, as examples to illustrate the  
 106 results derived in §2. In this section, we also study the dependence of the pull-in  
 107 and pull-off instabilities and the resulted hysteretic energy loss on the machine  
 108 stiffness. We compare the theoretical predictions of our model with experimental  
 109 measurements and discuss some potential sources for the discrepancies between  
 110 our model and experiments in §4.

## 111 2. Adhesive elastic contact model

### 112 2.1. Geometry

113 Figure 3 shows the geometry of our contact mechanics problem. Our problem  
 114 has the three-dimensional Euclidean point space  $\mathbb{E}^3$  as its backdrop. We identify  
 115 points in  $\mathbb{E}^3$  using the set of Cartesian coordinates  $\{x, y, z\}$  that correspond to  
 116 a fixed, orthonormal set of vectors  $\{\hat{e}_x, \hat{e}_y, \hat{e}_z\}$  that span the vector space  $\mathcal{V}$   
 117 associated with  $\mathbb{E}^3$ .

118 The tip in the class of experiments that we model in this paper is usually  
 119 composed of materials that are much stiffer than that of the substrate. Thus,  
 120 we model the tip as a rigid solid. Recall that in the experiments we model, the  
 121 tip's geometry has continuous rotational symmetry. Therefore, we take the tip  
 122 to be a solid of revolution whose symmetry axis is a fixed line that is parallel  
 123 to  $\hat{e}_z$  and passes through the fixed point  $\mathcal{O}$ , which is the origin of  $\mathbb{E}^3$ . In the  
 124 reference configuration of our problem (Figure 3a), the tip's surface facing the  
 125 substrate is the region

$$\partial\mathcal{T}_0 := \{\mathcal{P}_t = \mathcal{O} + r\hat{e}_r(\theta) + f(r)\hat{e}_z \in \mathbb{E}^3 \mid \theta \in [0, 2\pi) \text{ and } r \in [0, \infty)\},$$

126 where the tip's radial profile  $f : [0, \infty) \rightarrow (-\infty, 0]$  is a sufficiently smooth  
 127 function such that  $f(0) = 0$ , the vector  $\hat{e}_r(\theta) := \cos\theta\hat{e}_x + \sin\theta\hat{e}_y$ , and  $r$  and  $\theta$   
 128 are, respectively, the radial and polar coordinates of  $\mathcal{P}_t$ .

129 We model the instrument's stage as a material point and the structure con-  
 130 necting the tip and the stage as a linear elastic spring. In the reference confi-  
 131 guration of Figure 3a, the spring is unstretched. In the class of experiments we  
 132 model, the size of the contact region is typically much smaller than the dimen-  
 133 sions of the substrate. In the reference configuration, the substrate occupies the  
 134 region  $z \geq 0$ , which we refer to as the half-space  $\mathcal{S}_0$ . We refer to the surface of  
 135  $\mathcal{S}_0$  that faces the tip as  $\partial\mathcal{S}_0$ . In the reference configuration, there is no contact  
 136 between the tip and substrate and the substrate is stress-free. We discuss in  
 137 more detail what it means for the tip and substrate to be in contact later in  
 138 this section.

139 Figure 3b shows the deformed configuration of our problem. In it, the stage  
 140 and tip have been moved by amounts of  $\Delta\hat{e}_z$  and  $h\hat{e}_z$ , respectively, from where  
 141 they were located in the reference configuration. We call  $\Delta$  the stage displace-  
 142 ment and  $h \in (-\infty, +\infty)$  the indentation depth. In the deformed configura-  
 143 tion, the tip's surface facing the substrate occupies the region

$$\partial\mathcal{T}_t := \{O + r\hat{e}_r(\theta) + \tilde{u}_z(r; h)\hat{e}_z \in \mathbb{E}^3 \mid \theta \in [0, 2\pi) \text{ and } r \in [0, \infty)\},$$

144 where  $\tilde{u}_z(\cdot, h) : [0, \infty) \rightarrow (-\infty, +\infty)$  is defined as

$$\tilde{u}_z(r; h) := h + f(r). \quad (2.1)$$

145 As is standard in continuum mechanics, we identify material particles that  
 146 belong to the tip or substrate by the spatial points in the reference configuration  
 147  $\mathbb{E}^3$  where they originate. We say that a substrate's surface material particle  
 148  $\mathcal{S} \in \partial\mathcal{S}_0$  is a contact particle if there exists a tip material particle  $\mathcal{Q} \in \partial\mathcal{T}_0$   
 149 such that  $\mathcal{S}$  and  $\mathcal{Q}$  occupy the same spatial point in the deformed configuration.  
 150 We refer to the set of all contact particles as the contact region  $\Gamma_c$  and to the  
 151 measure of  $\Gamma_c$  as the contact area. We define the tip and substrate to be in  
 152 contact if the contact area is strictly positive. As previously noted, our problem  
 153 is axisymmetric and the contact region in it is simply connected. Therefore, we  
 154 can always write  $\Gamma_c = \{\mathcal{S} \in \partial\mathcal{S}_0 \mid r \leq a\}$ , where  $r$  is  $\mathcal{S}$ 's radial coordinate and  
 155  $a \geq 0$  is  $\Gamma_c$ 's contact radius.

156 Let  $\mathcal{P} \in \mathcal{S}_0$  be a substrate material particle. The displacement of  $\mathcal{P}$  is the  
 157 vector  $\mathbf{u}(\mathcal{P})$  that is defined such that  $\mathcal{P} + \mathbf{u}(\mathcal{P}) = p$ , where  $p$  is  $\mathcal{P}$ 's location in  
 158 the deformed configuration. In our problem we only consider displacement fields  
 159  $\mathbf{u} : \mathcal{S}_0 \rightarrow \mathcal{V}$  for which  $p$  has the same  $\theta$  coordinate as  $\mathcal{P}$ . Therefore,  $\mathbf{u}(\mathcal{P})$  can  
 160 be expressed as  $u_r(r, z)\hat{e}_r(\theta) + u_z(r, z)\hat{e}_z$ , where  $r$ ,  $\theta$ , and  $z$  are  $\mathcal{P}$ 's cylindrical  
 161 coordinates and  $u_r(\cdot, \cdot), u_z(\cdot, \cdot) : [0, \infty) \times [0, \infty) \rightarrow (-\infty, \infty)$ .

162 Let  $\mathcal{S} \in \partial\mathcal{S}_0$  be a contact particle that is in contact with a tip particle  
 163  $\mathcal{Q} \in \partial\mathcal{T}_0$ . Because  $\mathcal{S}$  and  $\mathcal{Q}$  occupy the same spatial point in the deformed  
 164 configuration, it follows that

$$(r_S + u_r(r_S, 0))\hat{e}_r(\theta_S) + u_z(r_S, 0)\hat{e}_z = r_Q\hat{e}_r(\theta_Q) + \tilde{u}_z(r_Q; h)\hat{e}_z, \quad (2.2)$$

165 where  $r_S, \theta_S$  and  $r_Q, \theta_Q$  are the radial and polar coordinates of  $\mathcal{S}$  and  $\mathcal{Q}$ , respec-  
 166 tively. It follows from (2.2) that  $\theta_S = \theta_Q$ ,  $r_S + u_r(r_S, 0) = r_Q$ , and

$$u_z(r_S, 0) = \tilde{u}_z(r_S + u_r(r_S, 0); h). \quad (2.3)$$

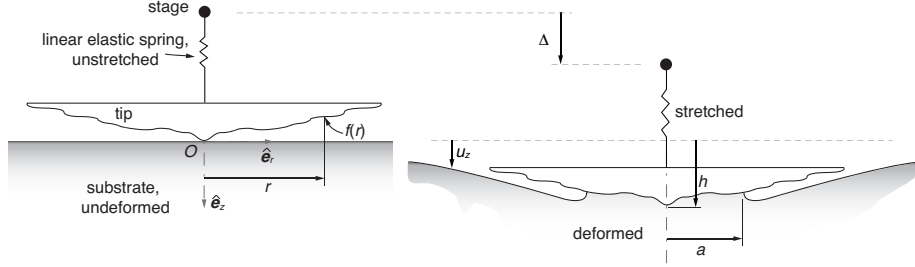


Figure 3: (a) and (b), respectively, show the reference and a deformed configuration of the contacting solids in our problem, see §2.1.

167 Imposing the boundary condition (2.3) on the substrate's displacement field  
 168 leads to a problem for which obtaining an analytical solution is quite challenging.  
 169 In our problem, we impose the boundary condition

$$u_z(r_S, 0) = \tilde{u}_z(r_S; h), \quad (2.4)$$

170 which is an approximation of (2.3) on the substrate's displacement field.

## 171 2.2. Variational formulation of the adhesive elastic contact problem

172 We use a variational perspective in the study of our contact mechanics problem.  
 173 That is, for a given stage displacement  $\Delta$ , we posit that the experimentally  
 174 observed configuration of the spring, tip, and half-space is one in which the system's  
 175 total energy is locally minimized with respect to  $a$ ,  $h$ , and  $\mathbf{u}$ . Thus, we  
 176 allow for the possibility of there being more than one configuration that is experimentally  
 177 observable at a given  $\Delta$ . We assume that the type of solutions we seek can be obtained  
 178 by first minimizing the potential energy with respect to  $\mathbf{u}$  alone, while holding  $a$  and  $h$   
 179 fixed, and then minimizing this partially minimized potential energy with respect to  
 180  $a$  and  $h$ .

181 The potential energy in our problem consists of three terms: the energy stored in the  
 182 spring because of its stretching, the energy stored in the contact region due to the  
 183 adhesive interactions between the tip and the substrate, and the energy stored in the  
 184 substrate due to its deformation. The potential energy stored in the spring that  
 185 connects the tip to the stage is  $k_s(\Delta - h)^2/2$ , where  $k_s \in (0, \infty)$  is the spring's  
 186 stiffness. As previously noted, we model adhesion between the tip and the substrate  
 187 using the JKR theory. According to this theory, the potential energy from the  
 188 adhesive interactions between the tip and substrate is  $-\pi w a^2$ . We model the  
 189 substrate as a homogeneous, isotropic, linear elastic material with Young's modulus  
 190  $E$  and Poisson's ratio  $\nu$ . Therefore, the potential energy stored in the substrate is  
 191

$$\frac{1}{2} \int_{S_0} \boldsymbol{\sigma} : \boldsymbol{\epsilon} dS_0, \quad (2.5)$$

192 where

$$\boldsymbol{\sigma} = \frac{E}{(1+\nu)} \left[ \boldsymbol{\epsilon} + \frac{\nu}{(1-2\nu)} \text{Tr}(\boldsymbol{\epsilon}) \mathbf{I} \right] \quad (2.6)$$

193 is the Cauchy stress tensor and

$$\boldsymbol{\epsilon} = \frac{1}{2} (\nabla \mathbf{u} + \nabla \mathbf{u}^\top) \quad (2.7)$$

194 is the small strain tensor. The symbol  $:$  in (2.5) denotes double contraction. In  
 195 (2.6), the symbol  $\mathbf{I}$  denotes the second rank identity tensor and  $\text{Tr}(\cdot)$  denotes  
 196 the trace operator. In (2.7) the operators  $\nabla(\cdot)$  and  $(\cdot)^\top$  denote the gradient and  
 197 transpose operators, respectively.

198 It follows from (2.4) that the displacement field always needs to satisfy the  
 199 essential boundary condition

$$u_z(r, 0) = \tilde{u}_z(r; h) \quad \text{on} \quad \Gamma_c. \quad (2.8)$$

200 When  $\Delta$ ,  $a$ , and  $h$  are held fixed, it can be shown that among the displacement  
 201 fields that satisfy (2.8), the one that minimizes the system's potential energy is  
 202 the one that satisfies the equation and boundary conditions

$$\text{Div}(\boldsymbol{\sigma}) = \mathbf{o} \quad \text{in} \quad \mathcal{S}_0, \quad (2.9a)$$

$$\boldsymbol{\sigma} \hat{\mathbf{e}}_z = \mathbf{o} \quad \text{on} \quad \partial \mathcal{S}_0 \setminus \Gamma_c, \quad (2.9b)$$

$$(\mathbf{I} - \hat{\mathbf{e}}_z \otimes \hat{\mathbf{e}}_z) \boldsymbol{\sigma} \hat{\mathbf{e}}_z = \mathbf{o} \quad \text{on} \quad \Gamma_c, \quad (2.9c)$$

203 where  $\text{Div}(\cdot)$  is the divergence operator,  $\mathbf{o}$  is the null vector in  $\mathcal{V}$ , and  $\hat{\mathbf{e}}_z \otimes \hat{\mathbf{e}}_z$   
 204 is the tensor product of  $\hat{\mathbf{e}}_z$  and itself. It is also required that the components  
 205 of  $\mathbf{u}$  and  $\boldsymbol{\sigma}$ , respectively, be asymptotic to  $(r^2 + z^2)^{-1/2}$  and  $(r^2 + z^2)^{-1}$  as  
 206  $(r^2 + z^2)^{1/2} \rightarrow \infty$ .

207 The solution to the mixed boundary value problem defined by (2.8)–(2.9)  
 208 was given by Sneddon [34]. (For a concise derivation of this solution using  
 209 Betti's reciprocity theorem, see [35].) Using that solution, it can be shown that  
 210 for any given  $\Delta$  and  $h$  and a positive  $a$ , the partially minimized potential energy  
 211 of the system is

$$\frac{\pi^2 E}{4(1-\nu^2)} \int_0^a \chi(\tilde{a}; h)^2 d\tilde{a} + \frac{1}{2} k_s (\Delta - h)^2 - \pi w a^2, \quad (2.10)$$

212 where

$$\chi(\tilde{a}; h) = \frac{2}{\pi} \left[ h + \tilde{a} \int_0^{\tilde{a}} \frac{\tilde{u}'_z(r; h)}{\sqrt{\tilde{a}^2 - r^2}} dr \right] \quad \text{for} \quad \tilde{a} > 0. \quad (2.11)$$

213 Because of the boundary condition (2.8), the mixed boundary value problem  
 214 defined by is not well posed when  $a = 0$  and  $h \neq 0$ . The value of the expression  
 215 (2.10) equals the system's partially minimized potential energy only when  $a > 0$   
 216 or when  $a = 0$  and  $h = 0$ . When  $a = 0$  and  $h \leq 0$ , the tip and the half-space  
 217 are not in contact. In this case, the partially minimized potential energy only

218 results from the stretching or compression of the spring. It is not possible for  
 219  $a = 0$  and  $h > 0$  because the tip cannot move into the region that is occupied  
 220 by the unstressed half-space without forming any contact area with the half-  
 221 space. Therefore, we conclude that the variational solution we seek will remain  
 222 unaltered if we take the partially minimized potential energy of the system to  
 223 be given by the value of the function  $\Pi(\cdot, \cdot; \Delta) : \mathcal{D} \subset \mathbb{R}^2 \rightarrow \mathbb{R} \cup +\infty$ , where

$$\Pi(a, h; \Delta) := \begin{cases} \frac{\pi^2 \mathcal{E}}{4} \int_0^a \chi(\tilde{a}; h)^2 d\tilde{a} + \frac{1}{2} k_s (\Delta - h)^2 - \pi w a^2, & a > 0, h \in (-\infty, +\infty), \\ \frac{1}{2} k_s (\Delta - h)^2, & a = 0, h \leq 0, \\ +\infty, & a = 0, h > 0, \end{cases} \quad (2.12)$$

224 with the domain

$$\mathcal{D} := [0, \infty) \times (-\infty, +\infty), \quad (2.13)$$

225 and the plane strain Young's modulus  $\mathcal{E} := E/(1-\nu^2)$ . We next locally minimize  
 226  $\Pi(\cdot, \cdot; \Delta)$  with respect to  $a$  and  $h$ . More precisely, we seek the solution point  
 227  $(a^*, h^*) \in \mathcal{D}$  for which there exists a positive number  $\delta$  such that

$$\Pi(a^*, h^*; \Delta) \leq \Pi(a, h; \Delta), \quad \forall (a, h) \in B(a^*, h^*, \delta), \quad (2.14)$$

228 where  $B(a^*; h^*; \delta) := \{(a, h) \in \mathbb{R}^2 \mid \|(a^*, h^*) - (a, h)\| < \delta\}$ . The solution point  
 229 is also said to be the stable equilibrium configuration of the adhesive elastic  
 230 contact.

### 231 2.3. Solutions

#### 232 2.3.1. Contact radius and indentation depth

233 The solutions defined by (2.14) can lie either in the interior of the domain  
 234 or on its boundary. We name the points in the interior of  $\mathcal{D}$  *interior points*  
 235 and on the boundary of  $\mathcal{D}$  *boundary points*. We denote the boundary of  $\mathcal{D}$  as  
 236  $\text{int}(\mathcal{D})$  and the interior of  $\mathcal{D}$  as  $\partial\mathcal{D}$ . It follows from the definition of  $\mathcal{D}$  that  
 237 the interior and boundary points are simply the points  $(a, h) \in \mathbb{R}^2$  with  $a > 0$   
 238 and  $a = 0$ , respectively. We show in [Appendix A](#) that the boundary contains  
 239 solutions only when  $\Delta < 0$ , and that those solutions are of the form  $(0, \Delta)$ . In  
 240 the remainder of this section, we only discuss solution points that lie in  $\text{int}(\mathcal{D})$ .  
 241 We begin by defining and characterizing the stationary points that are relevant  
 242 for our discussion of interior solution points.

243 *Stationary points.* A stationary point  $(a^\circ, h^\circ)$  is an interior point that satisfies  
 244 the first order conditions

$$\frac{\partial \Pi}{\partial h}(a^\circ, h^\circ; \Delta) = 0, \quad (2.15a)$$

$$\frac{\partial \Pi}{\partial a}(a^\circ, h^\circ; \Delta) = 0. \quad (2.15b)$$

245 The stationary point is also referred to as the equilibrium configuration of the  
 246 adhesive elastic contact. At all interior points  $(a, h)$  it follows from (2.12) that

$$\frac{\partial \Pi}{\partial h}(a, h; \Delta) = \frac{\pi^2 \mathcal{E}}{2} \int_0^a \chi(\tilde{a}; h) \frac{\partial \chi(\tilde{a}; h)}{\partial h} d\tilde{a} - k_s(\Delta - h), \quad (2.16a)$$

$$\frac{\partial \Pi}{\partial a}(a, h; \Delta) = \frac{\pi^2 \mathcal{E}}{4} \chi(a; h)^2 - 2\pi a w. \quad (2.16b)$$

247 At any interior point  $(a, h)$  it follows from (2.11) that  $\partial \chi(a; h)/\partial h = 2/\pi$ .  
 248 Thus, after substituting  $\partial \chi(\tilde{a}; h)/\partial h$  with  $2/\pi$  in (2.16a) and simplifying, we  
 249 find that

$$\frac{\partial \Pi}{\partial h}(a, h; \Delta) = \pi \mathcal{E} \int_0^a \chi(\tilde{a}; h) d\tilde{a} - k_s(\Delta - h). \quad (2.17)$$

250 Equations (2.15a) and (2.17) imply that

$$\pi \mathcal{E} \int_0^{a^\circ} \chi(\tilde{a}; h^\circ) d\tilde{a} - k_s(\Delta - h^\circ) = 0. \quad (2.18)$$

251 Equations (2.15b) and (2.16b) imply that  $\chi(a^\circ; h^\circ)$  is equal to  $\pm \sqrt{8a^\circ w/(\pi \mathcal{E})}$ .  
 252 However, we show in Appendix B that only the negative square root is physically  
 253 meaningful, i.e.,

$$\chi(a^\circ; h^\circ) = -\sqrt{\frac{8a^\circ w}{\pi \mathcal{E}}}. \quad (2.19)$$

254 Equivalently, the stationary point  $(a^\circ, h^\circ)$  is a root of the function

$$(a, h) \mapsto \chi(a; h) + \sqrt{\frac{8aw}{\pi \mathcal{E}}}. \quad (2.20)$$

255 It follows from (2.11) and (2.20) and the *implicit function theorem* that there  
 256 exists a function  $\hat{h}$  that is defined on a neighborhood of  $a^\circ$  such that

$$h^\circ = \hat{h}(a^\circ). \quad (2.21)$$

257 We derive  $\hat{h}$  for contact experiments involving a spherical and conical tip in §3.1  
 258 and §3.2, respectively.

259 *First order necessary condition.* It can be shown that  $\Pi(\cdot, \cdot; \Delta)$  is continuously  
 260 differentiable on  $\text{int}(\mathcal{D})$ . Consequently, if  $(a^*, h^*)$  is an interior solution point,  
 261 then it must also be a stationary point. Therefore, an interior solution point  
 262  $(a^*, h^*)$  is also a root of the function (2.20) and it satisfies the equation  $h^* =$   
 263  $\hat{h}(a^*)$ .

264 *Second order necessary condition.* We discuss the second order conditions in Ap-  
 265 pendix C. A consequence of those conditions is that the value of the function  
 266  $g : [0, \infty) \rightarrow \mathbb{R}$ , where

$$g(a) := \hat{h}'(a) - \frac{\sqrt{8\pi a \mathcal{E} w}}{2a \mathcal{E} + k_s} \quad (2.22)$$

267 at an interior solution point's abscissa should be non-negative. The derivative  
 268 of  $\hat{h}$  is denoted as  $\hat{h}'$ .

269 *Second order sufficient condition.* We show in [Appendix C.3.1](#) that a stationary  
 270 point  $(a^\circ, h^\circ)$  is a solution point if

$$g(a^\circ) > 0. \quad (2.23)$$

271 Equation (2.23) is the second order sufficiency condition (C.12) written in terms  
 272 of the function  $g$ , which we introduced in (2.22).

### 273 2.3.2. Contact force

274 In our contact problem, the contact force between the tip and the substrate  
 275 can be written as  $P\hat{e}_z$ . When  $P$  is non-negative (resp. non-positive), we say  
 276 that the contact force is compressive (resp. attractive). The contact force  
 277 corresponding to the solution point  $(a^*, h^*)$  is denoted as  $P^*$ .

278 As we discussed in §2.3.1, the solution points  $(a^*, h^*)$  belonging to  $\partial\mathcal{D}$  are of  
 279 the form  $(0, \Delta)$ , where  $\Delta < 0$ . In the solutions corresponding to those points,  
 280 the spring is unstretched, the substrate is undeformed, and the tip and the  
 281 substrate are not in physical contact. (See [Appendix A](#) for details.) Therefore,  
 282 the contact force  $P^* = 0$  in those solutions.

283 When  $(a^*, h^*)$  belongs to the  $\text{int}(\mathcal{D})$  it follows from the results presented by  
 284 Sneddon [34] and [35, 5.10] that the contact force  $P^*$  is

$$P^* = \mathcal{P}(a^*, h^*), \quad (2.24a)$$

285 where  $\mathcal{P} : \mathcal{D} \rightarrow \mathbb{R}$  and

$$\mathcal{P}(a, h) := \pi\mathcal{E} \int_0^a \chi(r; h) dr. \quad (2.24b)$$

286 As we discussed in §2.3.1, by necessity an interior solution point is also a sta-  
 287 tionary point. Thus, we can replace  $a^\circ$  and  $h^\circ$  with, respectively,  $a^*$  and  $h^*$   
 288 in (2.18) and (2.19), and then, from (2.24), substitute  $\pi\mathcal{E} \int_0^{a^*} \chi(\tilde{a}; h^*) d\tilde{a}$  with  
 289  $P^*$  in the first of the resulting equations to get

$$\Delta = \frac{P^*}{k_s} + h^* \quad (2.25)$$

290 and

$$\chi(a^*; h^*) = -\sqrt{\frac{8a^*w}{\pi\mathcal{E}}}. \quad (2.26)$$

291 We determine the solution contact radius, indentation depth, and contact force,  
 292 i.e.,  $a^*$ ,  $h^*$ , and  $P^*$ , through simultaneously solving the equations (2.24a)–(2.26).

293 We illustrate this in §3.1 and §3.2, respectively, where we consider tips having  
 294 spherical and conical shapes.

295 **3. Applications**

296 *3.1. Spherical tip*

297 *3.1.1. Theory*

298 In AFM-type contact experiments involving a substrate that is especially  
 299 delicate, such as a gel or a biological tissue, it is customary to use a spherical  
 300 glass or polystyrene bead as the tip [20–23]. The radial profile of the spherical  
 301 tip can be written as

$$f(r) = R(1 - r^2/R^2)^{1/2},$$

302 where  $0 \leq r < R$  and  $R$  is the sphere’s radius, see Figure 4a. For this particular  
 303  $f$  on calculating  $\tilde{u}_z$  from (2.1) and substituting it into (2.11), we get

$$\chi(\tilde{a}; h) = \frac{2}{\pi} \left[ h - \tilde{a} \tanh^{-1} \left( \frac{\tilde{a}}{R} \right) \right]. \quad (3.1)$$

304 From (3.1), it follows that in the limit  $\tilde{a}/R \rightarrow 0$

$$\frac{\chi(\tilde{a}; h)}{R} = \frac{2}{\pi} \left[ \frac{h}{R} - \left( \frac{\tilde{a}}{R} \right)^2 \right] + O \left( \frac{\tilde{a}^4}{R^4} \right). \quad (3.2)$$

305 Generally, when measuring compliant materials, the contact radius must be  
 306 made large enough that the contact force is measurable. Because of this, during  
 307 some stages of the experiments the contact radius  $a$  is not substantially smaller  
 308 than the bead radius  $R$ . Despite that, in order to simplify some of the ensuing  
 309 calculations in this section, we assume that the contact radius during the ex-  
 310 periment is much smaller than  $R$ . That is, we ignore the fourth order term in  
 311 (3.2) and simply take

$$\chi(\tilde{a}; h) = \frac{2}{\pi} \left( h - \frac{\tilde{a}^2}{R} \right). \quad (3.3)$$

312 Substituting (3.3) in (2.18) and (2.19), we find that the points  $(a^\circ, h^\circ)$  satisfy  
 313 the equations

$$h^\circ = \mathfrak{h}(a^\circ), \quad (3.4a)$$

314 where

$$\mathfrak{h}(a^\circ) = \frac{a^{\circ 2}}{R} - \sqrt{\frac{2\pi a^\circ w}{\mathcal{E}}} \quad (3.4b)$$

315 and

$$\Delta = \frac{\mathcal{P}(a^\circ, h^\circ)}{k_s} + h^\circ, \quad (3.5a)$$

316 where

$$\mathcal{P}(a^\circ, h^\circ) = 2a^\circ h^\circ \mathcal{E} - \frac{2a^{\circ 3} \mathcal{E}}{3R}. \quad (3.5b)$$

317 Recall from §2.3 that a stationary point  $(a^\circ, h^\circ)$  is a solution point if it  
 318 satisfies the condition (2.23). We can compute the derivative of the function  $\hat{h}$   
 319 given in (3.4b) and substitute it into (2.22) to determine the function  $g$ , and  
 320 then substitute  $g$  in (2.23). In doing this, we find that  $(a^\circ, h^\circ)$  is a solution  
 321 point if

$$g(a^\circ) = \frac{2a^\circ}{R} - \sqrt{\frac{\pi w}{2a^\circ \mathcal{E}}} - \frac{\sqrt{8\pi a^\circ \mathcal{E} w}}{2a^\circ \mathcal{E} + k_s} \quad (3.6)$$

322 is positive.

323 The non-dimensional variables and parameters  $\bar{\mathcal{P}}(\bar{a}^\circ, \bar{h}^\circ) := \mathcal{P}(a^\circ, h^\circ)/\hat{P}$ ,  
 324  $\bar{h}(\bar{a}^\circ) := \hat{h}(a^\circ)/\hat{h}$ , and  $\bar{\Delta} = \Delta/\hat{h}$ , where  $\bar{a}^\circ = a^\circ/\hat{a}$ ,  $\bar{h}^\circ = h^\circ/\hat{h}$ ,  $\hat{P} := 3\pi w R/2$ ,  
 325  $\hat{a} := (9\pi w R^2/8\mathcal{E})^{1/3}$ , and  $\hat{h} := (\hat{a}^2/R)$  allow equations (3.4)–(3.5) to be written  
 326 as, respectively,

$$\bar{h}^\circ = \bar{h}(\bar{a}^\circ), \quad (3.7a)$$

327 where

$$\bar{h}(\bar{a}^\circ) = \bar{a}^{\circ 2} - \frac{4}{3}\bar{a}^{\circ 1/2} \quad (3.7b)$$

328 and

$$\bar{\Delta} = \frac{4}{3\alpha}\bar{\mathcal{P}}(\bar{a}^\circ, \bar{h}^\circ) + \bar{h}^\circ, \quad (3.8a)$$

329 where

$$\bar{\mathcal{P}}(\bar{a}^\circ, \bar{h}^\circ) = \frac{3}{2}\bar{a}^\circ \bar{h}^\circ - \frac{1}{2}\bar{a}^{\circ 3}. \quad (3.8b)$$

330 Defining  $\bar{g}(\bar{a}^\circ) := \bar{a}^{\circ 1/2} g(\bar{a}^\circ \hat{a})/(3\pi w/(8\mathcal{E}R))^{1/3}$  and with the non-dimensional  
 331 parameters  $\hat{a}$  and  $\alpha$ , we get from (3.6) that

$$\bar{g}(\bar{a}^\circ) = 3\bar{a}^{\circ 3/2} - \frac{4\bar{a}^\circ}{2\bar{a}^\circ + \alpha} - 1. \quad (3.9)$$

332 The parameter  $\alpha$  in (3.8a) and (3.9) is the ratio of the machine stiffness  $k_s$  to  
 333 the contact interface's characteristic stiffness  $\hat{k}_s := (9\pi w \mathcal{E}^2 R^2/8)^{1/3}$ .

### 334 3.1.2. Numerical calculation of pull-in and pull-off forces and hysteretic energy 335 loss

336 We numerically computed the stationary points for a range of  $\bar{\Delta}$  values  
 337 using (3.7)–(3.8). The results from these calculations are shown in Figure 4b–c.  
 338 It follows from the discussion in Appendix A that the pull-in instability occurs  
 339 when  $\bar{\Delta} = 0$ . The contact radius just after the pull-in instability,  $\bar{a}_i$ , is the  
 340 abscissa of the stationary point that satisfies (3.7)–(3.8) for  $\bar{\Delta}=0$ . We define the  
 341 pull-off contact radius  $\bar{a}_o$  to be  $\arg \inf \{\bar{a}^\circ \mid \bar{g}(\bar{a}^\circ) > 0\}$ . The indentation-depths  
 342 just prior to the pull-in instability and pull-off instability are, respectively,  $\bar{h}_i =$

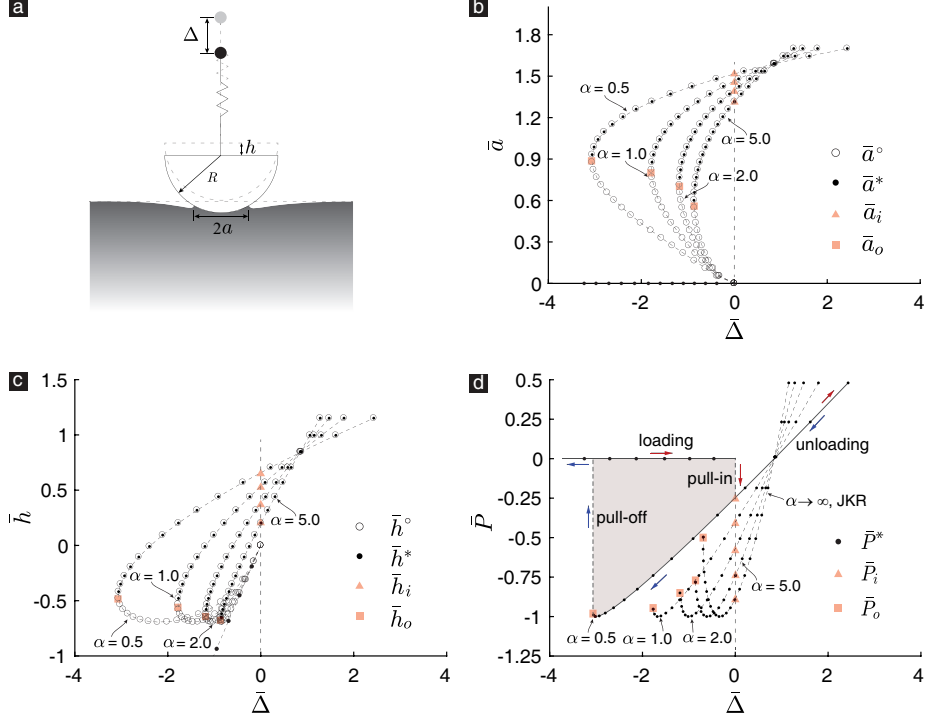


Figure 4: (a) Geometry of the spherical-tip contact problem. In (b)–(d) we denote the different tip-substrate configurations as points. A configuration’s abscissa gives its prescribed state displacement  $\bar{\Delta}$ . In (b) and (c) the ordinate of each configuration gives its contact radius and indentation depth, respectively. The configurations whose contact radii and indentation depths corresponding to stationary points are marked as circles, while those corresponding to solution points are marked as dots. In (d) the ordinate of a configuration gives its contact force  $\bar{P}^*$ . The configurations just after the occurrence of the pull-in instability are marked by triangles, while the configurations just before the occurrence of the pull-off instability are marked by squares.

343  $\bar{h}(\bar{a}_i)$  and  $\bar{h}_o = \bar{h}(\bar{a}_o)$ , where  $\bar{h}$  for the spherical tip is given in (3.7b). We marked  
 344  $\bar{a}_i$  and  $\bar{a}_o$  in Figure 4b, and  $\bar{h}_i$  and  $\bar{h}_o$  in Figure 4c.

345 We define a non-dimensional solution point to be  $(\bar{a}^*, \bar{h}^*) := (a^*/\hat{a}, h^*/\hat{h})$ .  
 346 A stationary point  $(\bar{a}^\circ, \bar{h}^\circ)$  qualifies as a non-dimensional solution point if its  
 347 abscissa satisfies the sufficiency condition that  $\bar{g}(\bar{a}^\circ)$  in (3.9) is positive. We  
 348 show the abscissa and ordinate of several of these solution points in Figure 4a  
 349 and b, respectively, using solid symbols. In addition to the solution points that  
 350 we have from the set of stationary points, it follows from the discussion of §2.3.1  
 351 that when  $\bar{\Delta} < 0$  we have additional solution points on the boundary  $\partial\mathcal{D}$  that  
 352 are of the form  $(0, \bar{\Delta})$ . The abscissa and ordinate of these points are also marked  
 353 in Figure 4b and c, respectively.

354 For each of the solution points  $(\bar{a}^*, \bar{h}^*)$  shown in Figure 4b–c, we computed

355 the non-dimensional contact force  $\bar{P}^* := P^*/\hat{P}$  as  $\bar{\mathcal{P}}(\bar{a}^*, \bar{h}^*)$ , where  $\bar{\mathcal{P}}$  for the  
 356 spherical tip is given in (3.8b). We show these force values in Figure 4d. The  
 357 contact forces corresponding to the solution points of the form  $(0, \bar{\Delta})$ , which are  
 358 actually all zero, are also shown in that figure.

359 We denote the contact force and the stage displacement just prior to the  
 360 occurrence of the pull-in (resp. pull-off) instability as  $\bar{P}_i^*$  (resp.  $\bar{P}_o^*$ ) and  $\bar{\Delta}_i$   
 361 (resp.  $\bar{\Delta}_o$ ). Recall that  $\bar{\Delta}_i = 0$ . It follows from (3.8a) that

$$\bar{\Delta}_o = \frac{4}{3\alpha} \bar{\mathcal{P}}(\bar{a}_o, \bar{h}_o) + \bar{h}_o.$$

362 The pull-in and pull-off contact forces, i.e.  $\bar{P}_i^*$  and  $\bar{P}_o^*$ , can be calculated  
 363 as  $\bar{\mathcal{P}}(\bar{a}_i, \bar{h}_i)$  and  $\bar{\mathcal{P}}(\bar{a}_o, \bar{h}_o)$ , respectively, where  $\bar{\mathcal{P}}$  for the spherical tip is given  
 364 in (3.8b). We have marked the points  $(\bar{\Delta}_i, \bar{P}_i^*)$  and  $(\bar{\Delta}_o, \bar{P}_o^*)$  in Figure 4d.

365 We show the contact forces  $\bar{P}_i^*$  and  $\bar{P}_o^*$  as a function of  $\alpha$  in Figure 5a.  
 366 Through an analysis of (3.7) and (3.8), we found that as  $\alpha \rightarrow 0$  the contact forces  
 367  $\bar{P}_i^*$  and  $\bar{P}_o^*$  tend to 0 and  $-1$ , respectively. And as  $\alpha \rightarrow \infty$ , the contact forces  $\bar{P}_i^*$   
 368 and  $\bar{P}_o^*$  tend to  $-8/9$  and  $-5/9$ , respectively. With the aid of these asymptotic  
 369 results we were able to construct the functions  $\bar{\mathcal{P}}_i^*, \bar{\mathcal{P}}_o^* : (0, \infty) \rightarrow (-\infty, 0)$ ,  
 370 where

$$\bar{\mathcal{P}}_i^*(\alpha) = -\frac{8}{9} \left( 1 - \frac{1}{1 + 0.83\alpha^{1.12}} \right) \quad (3.10a)$$

371 and

$$\bar{\mathcal{P}}_o^*(\alpha) = -\frac{1}{9} \left( 5 + \frac{4}{1 + 0.21\alpha^{1.32}} \right). \quad (3.10b)$$

372 These provide excellent approximations for  $\bar{P}_i^*$  and  $\bar{P}_o^*$  for a wide range of  $\alpha$   
 373 values. (See Figure 5a.)

374 As can be noted from Figure 4b and c, there exist two solution points for  
 375 some  $\bar{\Delta}$  values. For those same values, unsurprisingly, there are also two force  
 376 values. Which of these two force values are actually measured in an experiment  
 377 depends on the contact cycle employed in that experiment. For example, for  
 378 the typical contact cycle discussed in §1, the experiment will measure the force  
 379 values that we have marked using right and left arrows in Figure 4d during the  
 380 loading and the unloading phases, respectively.

381 The hysteretic energy loss during a contact cycle can be computed as  
 382  $(R^4 w^5 / \mathcal{E}^2)^{1/3} \bar{H}$ , where

$$\bar{H} = \frac{4}{3\alpha} \int_{\bar{a}_o}^{\bar{a}_i} \bar{\mathcal{P}}(\bar{a}^*, \bar{h}(\bar{a}^*)) \left[ \bar{\mathcal{P}}_{,1}(\bar{a}^*, \bar{h}(\bar{a}^*)) + \bar{\mathcal{P}}_{,2}(\bar{a}^*, \bar{h}(\bar{a}^*)) \bar{h}'(\bar{a}^*) + \frac{3\alpha}{4} \bar{h}'(\bar{a}^*) \right] d\bar{a}^*, \quad (3.11)$$

383 in which  $\bar{\mathcal{P}}_{,1}$  and  $\bar{\mathcal{P}}_{,2}$  are the partial derivatives of  $\bar{\mathcal{P}}$  with respect to its first  
 384 and second arguments, respectively. It can be shown that as  $\alpha \rightarrow 0$  the  
 385 hysteretic energy loss  $\bar{H} \rightarrow \infty$ , and as  $\alpha \rightarrow \infty$  the hysteretic energy loss

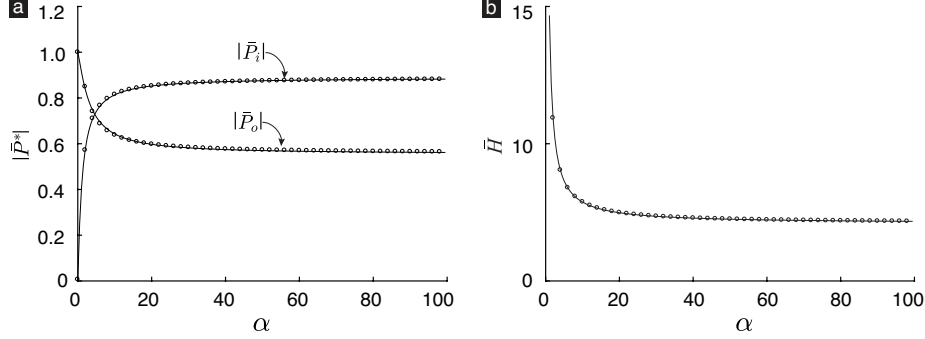


Figure 5: The spherical-tip case. (a) The exact (circles) and approximate (solid line) values of  $|\bar{P}_i|$  and  $|\bar{P}_o|$  as a function of  $\alpha$ . The exact values are computed using the procedure outlined in §3.1.2. The approximate values are given by the functions  $\bar{\mathcal{P}}_i$  and  $\bar{\mathcal{P}}_o$  defined in (3.10). (b) The exact (circles) and approximate (solid line) values of  $\bar{H}$  as a function of  $\alpha$ . The exact values are computed using (3.11), while the approximate values are given by the function  $\bar{\mathcal{H}}$  defined in (3.12).

386  $\bar{H} \rightarrow (\pi^{5/3} + 3(2\pi)^{5/3})/10 (\approx 7.092)$ . With the aid of these asymptotic re-  
 387 sults, we constructed the function  $\bar{\mathcal{H}} : (0, \infty) \rightarrow (0, \infty)$ , where

$$\bar{\mathcal{H}}(\alpha) = 7.092 + \frac{7.657}{\alpha^{0.99}}. \quad (3.12)$$

388 The values of  $\bar{\mathcal{H}}$  are very close to  $\bar{H}$  for a wide range of  $\alpha$  values, see Figure 5b.

### 389 3.2. Conical tip

#### 390 3.2.1. Theory

391 In this section, we consider a conical tip whose radial profile  $f(r) = -r \tan \theta$ ,  
 392 where  $\theta \in (0, \pi/2)$  is shown marked in Figure 6a. Calculating  $\tilde{u}_z$  from (2.1) for  
 393 this radial profile and substituting it into (2.11) results in

$$\chi(\tilde{a}; h) = \frac{2}{\pi} \left( h - \frac{\pi}{2} \tilde{a} \tan \theta \right). \quad (3.13)$$

394 As we did in the case of the spherical tip (§3.1), by substituting (3.13) in (2.18)–  
 395 (2.19) we obtain that the points  $(a^\circ, h^\circ)$  satisfy the equations

$$h^\circ = \hat{h}(a^\circ), \quad (3.14a)$$

396 where

$$\hat{h}(a^\circ) = 2a^\circ h^\circ \mathcal{E} - \frac{1}{2} \pi a^{\circ 2} \mathcal{E} \tan \theta \quad (3.14b)$$

397 and

$$\Delta = \frac{\mathcal{P}(a^\circ, h^\circ)}{k_s} + h^\circ, \quad (3.15a)$$

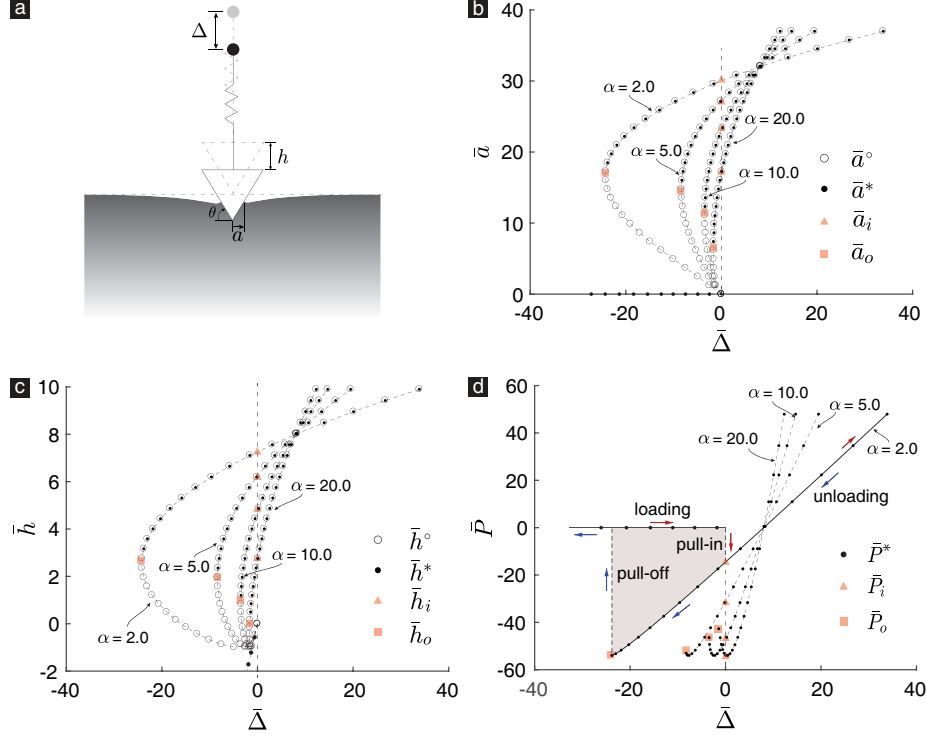


Figure 6: (a) Geometry of the conical-tip contact problem. In (b)–(d) we denote the different tip-substrate configurations as points. A configuration’s abscissa gives its prescribed state displacement  $\bar{\Delta}$ . In (b) and (c) the ordinate of each configuration gives its contact radius and indentation depth. The configurations whose contact radii and indentation depths corresponding to stationary points are marked as circles, while those that corresponding to solution points are marked as dots. In (d) the ordinate of a configuration gives its contact force  $\bar{P}^*$ . The configurations just after the occurrence of the pull-in instability are marked by triangles, while the configurations just before the occurrence of the pull-off instability are marked by squares.

398 where

$$\mathcal{P}(a^\circ, h^\circ) = 2a^\circ h^\circ \mathcal{E} - \frac{1}{2} \pi a^{\circ 2} \mathcal{E} \tan \theta. \quad (3.15b)$$

399 From (2.22) and (3.14b), it follows that the function  $g$  for the case of conical  
400 tip is

$$g(a^\circ) = \frac{\pi}{2} \tan \theta - \sqrt{\frac{\pi w}{2a^\circ \mathcal{E}}} - \frac{\sqrt{8\pi a^\circ \mathcal{E} w}}{2a^\circ \mathcal{E} + k_s}. \quad (3.16)$$

401 The functions with non-dimensional values and non-dimensional variables  
402  $\bar{\mathcal{P}}(\bar{a}^\circ, \bar{h}^\circ) := \mathcal{P}(a^\circ, h^\circ)/\hat{P}$ ,  $\bar{h}(\bar{a}^\circ) := h(a^\circ)/\hat{h}$ , and  $\bar{\Delta} := \Delta/\hat{h}$ , where  $\bar{a}^\circ := a^\circ/\hat{a}$ ,  
403  $\bar{h}^\circ := h^\circ/\hat{h}$ ,  $\hat{P} := w^2/(\pi \mathcal{E} \tan^3 \theta)$ ,  $\hat{a} := w/(\pi \mathcal{E} \tan^2 \theta)$ , and  $\hat{h} := w/(\mathcal{E} \tan \theta)$ ,

404 allow (3.14)–(3.15) to be written as, respectively,

$$\bar{h}^\circ = \bar{h}(\bar{a}^\circ), \quad (3.17a)$$

405 where

$$\bar{h}(\bar{a}^\circ) = \frac{\bar{a}^\circ}{2} - (2\bar{a}^\circ)^{1/2} \quad (3.17b)$$

406 and

$$\bar{\Delta} = \frac{1}{\alpha} \bar{\mathcal{P}}(\bar{a}^\circ, \bar{h}^\circ) + \bar{h}^\circ, \quad (3.18a)$$

407 where

$$\bar{\mathcal{P}}(\bar{a}^\circ, \bar{h}^\circ) = 2\bar{a}^\circ \bar{h}^\circ - \frac{1}{2} \bar{a}^{\circ 2}. \quad (3.18b)$$

408 The parameter  $\alpha$  in (3.18a) is the ratio of the machine stiffness  $k_s$  to the contact  
 409 interface's characteristic stiffness  $\hat{k}_s := w/(\pi \tan^2 \theta)$ . Defining  $\bar{g}(\bar{a}^\circ) :=$   
 410  $(2\bar{a}^\circ)^{1/2} g(\bar{a}^\circ \hat{a})/(\pi \tan \theta)$ , we find from (3.16) and the definitions of  $\alpha$  and  $\hat{a}$  that  
 411

$$\bar{g}(\bar{a}^\circ) = \frac{\sqrt{2\bar{a}^\circ}}{2} - \frac{4\bar{a}^\circ}{2\bar{a}^\circ + \alpha} - 1. \quad (3.19)$$

### 412 3.2.2. Numerical calculation of the pull-in and pull-off forces and the hysteretic 413 energy loss

414 We numerically computed the stationary points  $(\bar{a}^\circ, \bar{h}^\circ)$  for a range of  $\bar{\Delta}$   
 415 values using (3.17)–(3.18). The solution points  $(\bar{a}^*, \bar{h}^*)$  are those stationary  
 416 points  $(\bar{a}^\circ, \bar{h}^\circ)$  for which  $\bar{g}(\bar{a}^\circ) > 0$ , with  $\bar{g}$  being given in (3.19). When  $\bar{a}^* > 0$   
 417 then  $\bar{P}^* = \bar{\mathcal{P}}(\bar{a}^*, \bar{h}^*)$ , where  $\bar{\mathcal{P}}$  is given in (3.18b). When  $\bar{a}^* = 0$ , then  $\bar{P}^* = 0$ .  
 418 We show the abscissa (resp. ordinate) of the stationary and solution points as  
 419 a function of  $\bar{\Delta}$  in Figure 6b (resp. c), and show  $\bar{P}^*$  in Figure 6d.

420 We employed the same procedure that we used in §3.1 to identify the contact  
 421 radii  $\bar{a}_i$  and  $\bar{a}_o$ , indentation depths  $\bar{h}_i$  and  $\bar{h}_o$ , and contact forces  $\bar{P}_i$  and  $\bar{P}_o$  to  
 422 identify those quantities in the case of conical tip (Figure 6b–d). We found that  
 423 as  $\alpha \rightarrow 0$  the contact forces  $\bar{P}_i^*$  and  $\bar{P}_o^*$  approach 0 and  $-54$ , respectively. And  
 424 as  $\alpha \rightarrow \infty$ , the contact forces  $\bar{P}_i^*$  and  $\bar{P}_o^*$  approach  $-32$  and  $-6$ , respectively.  
 425 With the aid of these asymptotic results, we were able to construct the functions  
 426  $\bar{\mathcal{P}}_i^*$  and  $\bar{\mathcal{P}}_o^* : (0, \infty) \rightarrow (-\infty, 0)$ , where

$$\bar{\mathcal{P}}_i^*(\alpha) = -32 (1 - e^{-0.12\alpha}) \left( 1 + 2.05e^{-0.123\alpha^{0.665}} \right) \quad (3.20a)$$

427 and

$$\bar{\mathcal{P}}_o^*(\alpha) = -6 - \frac{48}{1 + 0.00158\alpha^{2.285}} \quad (3.20b)$$

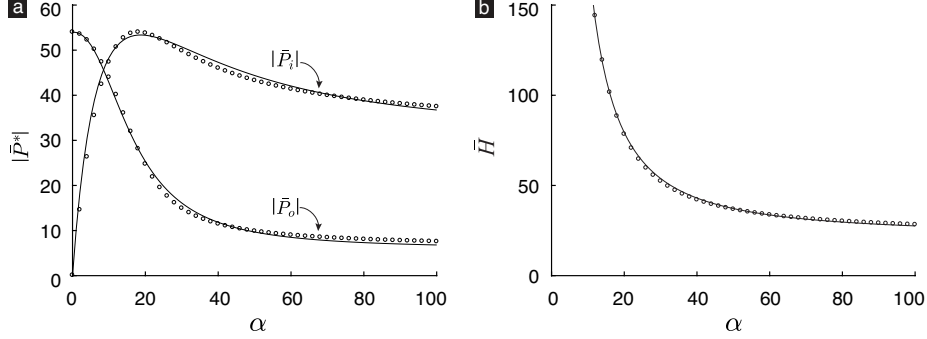


Figure 7: The conical-tip case. (a) The exact (circles) and approximate (solid line) values of  $|\bar{P}_i|$  and  $|\bar{P}_o|$  as a function of  $\alpha$ . The exact values are computed using the procedure outlined in §3.2.2. The approximate values are given by the functions  $\bar{\mathcal{P}}_i$  and  $\bar{\mathcal{P}}_o$  defined in (3.20). (b) The exact (circles) and approximate (solid line) values of  $\bar{H}$  as a function of  $\alpha$ . The exact values are computed using (3.21), while the approximate values are given by the function  $\bar{\mathcal{H}}$  defined in (3.22).

428 whose values approximate, respectively,  $\bar{P}_i^*$  and  $\bar{P}_o^*$  very closely for a wide range  
 429 of  $\alpha$  (Figure 7a).

430 We computed the hysteretic energy loss during a contact cycle as  
 431  $w^3 \bar{H} / (\pi \mathcal{E}^2 \tan^4 \theta)$ , where

$$\bar{H} = \frac{1}{\alpha} \int_{\bar{a}_o}^{\bar{a}_i} \bar{\mathcal{P}}(\bar{a}^*, \bar{h}(\bar{a}^*)) [\bar{\mathcal{P}}_{,1}(\bar{a}^*, \bar{h}(\bar{a}^*)) + \bar{\mathcal{P}}_{,2}(\bar{a}^*, \bar{h}(\bar{a}^*)) \bar{h}'(\bar{a}^*) + \alpha \bar{h}'(\bar{a}^*)] d\bar{a}^*, \quad (3.21)$$

432 in which  $\bar{h}$  and  $\bar{\mathcal{P}}$  are given in (3.17b) and (3.18b), respectively. We found that  
 433 as  $\alpha \rightarrow 0$  the hysteretic energy loss  $\bar{H} \rightarrow \infty$ , and as  $\alpha \rightarrow \infty$  the hysteretic  
 434 energy loss  $\bar{H} \rightarrow 22$ . With the aid of these asymptotic results we were able to  
 435 construct the function  $\bar{\mathcal{H}} : (0, \infty) \rightarrow (0, \infty)$ , where

$$\bar{\mathcal{H}}(\alpha) = 22 + \frac{4383.87}{\alpha^{1.4478}}, \quad (3.22)$$

436 whose value is very close to  $\bar{H}$  for a wide range of  $\alpha$  (Figure 7b).

## 437 4. Experimental comparison and discussion

### 438 4.1. Experimental comparison

439 In this section, we compare our model to the experiments reported by Sun *et*  
 440 *al.* [21] and Notbohm *et al.* [22]. Both experiments involved adhesive elastic  
 441 contact between a PDMS slab and an AFM tip. The AFM tip in Sun *et al.*'s  
 442 experiments was a  $\text{Si}_3\text{N}_4$  bead of radius  $R = 58$  nm. In Notbohm *et al.*'s  
 443 experiments the AFM tip was a glass bead with  $R = 2.5$   $\mu\text{m}$ .

444 In Figure 8a we show the contact force–indentation data from a repre-  
 445 sentative contact cycle in Sun *et al.*'s experiments as gray dots. In that same

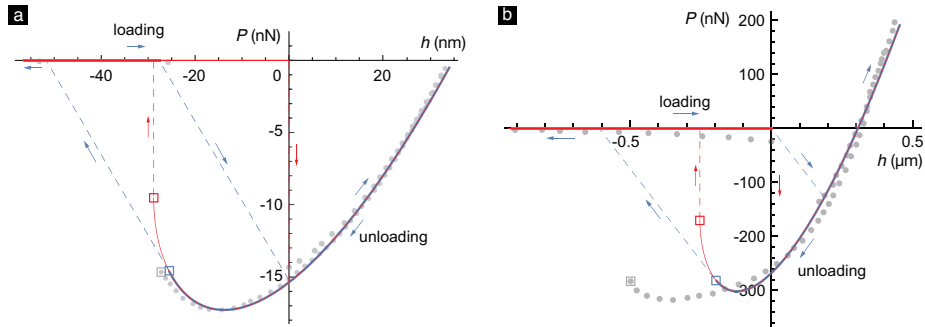


Figure 8: Comparison of the contact force–indentation depth curves predicted by our (blue lines) and the JKR (red lines) models with experimental data (gray dots). The data in (a) and (b) are, respectively, from the experiments performed by Sun *et al.* [21] and Notbohm *et al.* [22]. In each of the curves and data sets, the configuration just before the occurrence of the pull-off instability is marked with a square.

446 figure, we show the best fit of our model, specifically (3.4b) and (3.5b), as blue  
 447 curves and the JKR model as red curves. For both models, we use  $\mathcal{E}$  and  $w$   
 448 as the fitting parameters. (See Appendix D for details.) These parameters  
 449 come out to be 6.39 MPa and 63.2 mJ/m<sup>2</sup>, respectively, in the best fit of both  
 450 our model and the JKR model. Sun *et al.* [21] report the stiffness of the AFM  
 451 cantilever in their experiments to be  $k_s = 0.66$  N/m. Using this value, the best  
 452 fit of our model predicts the pull-off force to be  $-14.73$  nN, whereas the best fit  
 453 of the JKR model predicts it to be  $-5\pi wR/6 = -9.59$  nN. As can be seen in  
 454 Figure 8a, the experimental pull-off force is  $-14.8$  nN. Thus, the prediction of  
 455 the pull-off force from our model is much closer to the experimental value than  
 456 the prediction of the JKR model.

457 An important experimental feature that is uniquely captured by our model is  
 458 that in the experiments, the indentation depth changes by a finite amount during  
 459 the pull-in and pull-off instabilities. For example, in the data shown in Figure 8a,  
 460 the indentation depth changes by 26.7 nm and 26.9 nm during the pull-in and  
 461 pull-off instabilities, respectively. In alignment with these observations, the  
 462 best fit of our model predicts the indentation depth during the instabilities to  
 463 change by 27.4 nm and 26 nm, respectively. In distinct contrast, the JKR model  
 464 always predicts there to be no change in the indentation depth during either of  
 465 the instabilities.

466 Figure 8b shows the contact force–indentation depth data from a representa-  
 467 tive contact cycle in Notbohm *et al.*'s experiments as gray dots. The best fits  
 468 of our model and the JKR model are shown in Figure 8b as blue and red curves,  
 469 respectively. In the best fits of both our model and the JKR model,  $\mathcal{E}$  and  $w$   
 470 come out to be 0.65 MPa and 25.7 J/m<sup>2</sup>, respectively. The AFM cantilever's  
 471 stiffness in Notbohm *et al.*'s experiments was  $k_s = 0.642$  N/m. Using this value  
 472 for the machine stiffness, we find the pull-off contact force in the best fit of  
 473 our model to be  $-281.5$  nN. This value is remarkably close to the experimental

474 pull-off force value, which is  $-281.6$  nN. In contrast, the pull-off force in the best  
475 fit of the JKR theory is  $-5\pi wR/6 = -167.5$  nN, which is significantly greater  
476 than the experimental value. The changes in the indentation depth during the  
477 occurrence of the pull-in and pull-off instabilities in the experiments are  $0.17$   
478  $\mu\text{m}$  and  $0.41$   $\mu\text{m}$ , respectively. These changes in the best fit of our model are,  
479 respectively,  $0.19$   $\mu\text{m}$  and  $0.42$   $\mu\text{m}$ , which are very close to the experimental  
480 values.

#### 481 4.2. Discussion

482 There is a significant discrepancy between the best fits of our model, the  
483 JKR model, and the experiments towards the end of the unloading phase. (See  
484 Figure 8b.) Notbohm *et al.* [22] argue that the discrepancy between their data  
485 and the JKR model towards the end of the unloading phase was due to the  
486 nonlinear deformation behavior of the AFM cantilever. **However, we believe**  
487 **that this discrepancy requires further investigation.**

488 There is also a discrepancy between the best fits of our model, the JKR  
489 model, and Notbohm *et al.*'s experimental data just prior to the occurrence of  
490 the pull-in instability. Prior to the occurrence of the pull-in instability, there  
491 is no contact force in either our model or the JKR model. However, as can  
492 be noted in Figure 8b, in Notbohm *et al.*'s experiments there are some small,  
493 but non-negligible, negative contact forces prior to the occurrence of the pull-in  
494 instability. We believe that this discrepancy is due to the assumption in our  
495 model that the interbody adhesive interactions are infinitesimally short ranged.  
496 As we discussed in §1, dry adhesion mostly originates from van der Waals and  
497 Coulombic type interactions, which have a finite interaction range. The finite  
498 ranged interactions can give rise to negative forces between the tip and the  
499 substrate even prior to the occurrence of the pull-in instability. This view is  
500 supported by molecular statics simulations of adhesive elastic contact [36], in  
501 which the interbody interactions are taken to have a finite range and the contact  
502 forces in them are seen to be non-zero prior to the occurrence of the pull-in  
503 instability.

504 A further implication of our assumption that the interbody adhesive inter-  
505 actions are infinitesimally short ranged is that our model's prediction that the  
506 pull-in instability occurs when  $\Delta = 0$  is also quite likely to be inconsistent  
507 with experiments. In experiments, the pull-in instability is likely to occur when  
508  $\Delta < 0$ , although it might be difficult to experimentally demonstrate this fact  
509 since identifying the datum of  $\Delta$  is quite challenging in adhesive elastic contact  
510 experiments.

#### 511 Acknowledgment

512 This work was supported by the National Science Foundation through the  
513 Mechanics of Materials and Structures Program award number 1562656. Weilin  
514 Deng is partially supported by a graduate fellowship from the China Scholarship  
515 Council.

516 **Appendix A. Solutions on the boundary of the domain  $\mathcal{D}$**

517 In this section we study the solutions as defined by (2.14) that lie on the  
 518 boundary of the domain  $\mathcal{D}$  of the function  $\Pi(\cdot, \cdot; \Delta)$ . Recall that the domain  
 519 of  $\Pi(\cdot, \cdot; \Delta)$  is the set  $\mathcal{D} := \{(a, h) \in \mathbb{R}^2 : a \geq 0\}$ . Therefore, the domain  
 520 boundary  $\partial\mathcal{D}$  is simply the set of points in  $\mathbb{R}^2$  that are of the form  $(0, h)$ . As  
 521 we will show, the solution points on  $\partial\mathcal{D}$  could only exist in the form of  $(0, \Delta)$   
 522 when  $\Delta < 0$ . At these points, there is no deformation of the elastic spring and  
 523 the tip and the substrate are not in physical contact.

524 *Appendix A.1. Points of the form  $(0, h)$  where  $h > 0$  cannot be solutions*

525 A point of the form  $(0, h)$  where  $h > 0$  cannot be a solution to our contact  
 526 mechanics problem. Given any  $\delta > 0$ , the neighborhood  $B(0, h, \delta)$  of  $(0, h)$   
 527 contains the point  $(\delta/2, h)$ . The value of  $\Pi(\cdot, \cdot; \Delta)$  at  $(\delta/2, h)$ , as given by the  
 528 first line in (2.12), is finite and smaller than its value at  $(0, h)$ . As can be  
 529 determined by the third line of (2.12), it is also unbounded. That is, we are  
 530 always able to find a point in the neighborhood of  $(0, h)$ , no matter how small  
 531 the neighborhood's diameter, where the value of  $\Pi(\cdot, \cdot; \Delta)$  is smaller than at  
 532  $(0, h)$ . Consequently, the point  $(0, h)$  cannot be a solution.

533 *Appendix A.2. A point  $(a, h)$  where  $a = 0$  and  $h < 0$  is a solution iff  $\Delta < 0$  and*  
 534  $h = \Delta$

535 The difference in the value of  $\Pi(\cdot, \cdot; \Delta)$  at a point  $(0, h)$ , where  $h < 0$ , and a  
 536 neighboring point  $(\delta a, h + \delta h)$ , where  $\delta a \geq 0$ , can be expressed as

$$\Pi[\delta a, h + \delta h; \Delta] - \Pi[0, h; \Delta] = \mathcal{E}h^2\delta a + k_s\delta h(h - \Delta) + O(\|(\delta a, \delta h)\|^2) \quad (\text{A.1})$$

537 in the limit of  $(\delta a, \delta h) \rightarrow (0, 0)$ . Any sequence of points converging to  $(0, h)$   
 538 where  $h < 0$  can be expressed as  $(\delta a_n, h + \delta h_n)_{n \in \mathbb{N}}$ , where  $\delta a_n \geq 0$  and the  
 539 sequence  $(\delta a_n, \delta h_n)$  converges to  $(0, 0)$ . Consider the case  $\Delta < 0$  and  $h = \Delta$ .  
 540 It follows from (A.1) that there exists an  $N \in \mathbb{N}$  such that for all  $n > N$  the  
 541 sign of the difference  $\Pi[a_n, h_n; \Delta] - \Pi[0, h; \Delta]$  is the same as that of the leading  
 542 order term  $\mathcal{E}h^2\delta a_n$ . Because both  $\mathcal{E}$  and  $\delta a_n$  are positive, the leading order  
 543 term is positive. This result implies that when  $\Delta < 0$ , the point  $(0, \Delta)$  is always  
 544 a solution.

545 Now consider the case  $h \neq \Delta$  and the sequence of points  $(a_n, h_n)_{n \in \mathbb{N}}$  where  
 546  $a_n = 0$  and  $h_n = h - (h - \Delta)/n$ . This sequence of points also converge to  $(0, h)$ .  
 547 It follows from (A.1) that there exists an  $N \in \mathbb{N}$  such that for all  $n > N$  the  
 548 sign of the difference  $\Pi[a_n, h_n; \Delta] - \Pi[0, h; \Delta]$  is the as same that of the term  
 549  $-k_s(h - \Delta)^2/n$ , which is negative because  $k_s > 0$ . Therefore, when  $h \neq \Delta$ , the  
 550 point  $(0, h)$  where  $h < 0$  cannot be a solution. Therefore, it is implied that that  
 551 a point of the form  $(0, h)$  where  $h < 0$  is a solution iff  $\Delta < 0$  and  $h = \Delta$ .

552 *Appendix A.3. The point  $(a, h) = (0, 0)$  cannot be a solution*

553 In this section we show that the point  $(a, h) = (0, 0)$  cannot be a solution  
 554 at any given  $\Delta$ . We demonstrate this by showing that no matter how small  
 555  $\delta$  is, there will always exist points in  $B(0, 0, \delta)$  where the value of  $\Pi(\cdot, \cdot; \Delta)$  is  
 556 smaller than its value at  $(a, h) = (0, 0)$ . We begin by deriving an asymptotic  
 557 series expansion for  $\Pi(\cdot, \cdot; \Delta)$  in the limit  $(a, h) \rightarrow 0$ , with  $a > 0$ . In the limit  
 558  $\tilde{a} \rightarrow 0$  we know from (2.1) and (2.11) that

$$\chi(\tilde{a}; h) = \frac{2h}{\pi} + \tilde{a}f'(0) + \frac{2\tilde{a}^2}{\pi}f''(0) + O(\tilde{a}^3), \quad (\text{A.2})$$

559 where  $O$  is the Bachmann–Landau “Big-Oh” symbol. We then obtain

$$\chi(\tilde{a}; h)^2 = \frac{4h^2}{\pi^2} + \frac{4ahf'(0)}{\pi} + a^2 \left( \frac{8hf''(0)}{\pi^2} + f'(0)^2 \right) + O(\tilde{a}^3). \quad (\text{A.3})$$

560 After substituting (A.3) into (2.12) and simplifying, we determine that

$$\begin{aligned} \frac{\pi^2 \mathcal{E}}{4} \int_0^a \chi(\tilde{a}; h)^2 d\tilde{a} &= \mathcal{E}h^2 a + \frac{\pi}{2} \mathcal{E}h f'(0) a^2 \\ &+ \mathcal{E} \left( \frac{2}{3} h f''(0) + \frac{\pi^2}{12} f'(0)^2 \right) a^3 + O(a^4). \end{aligned} \quad (\text{A.4})$$

561 It follows that in the limit  $(a, h) \rightarrow (0, 0)$  with  $a > 0$ , the potential energy can  
 562 be written as

$$\begin{aligned} \Pi(a, h; \Delta) &= \frac{1}{2} k_s \Delta^2 - k_s \Delta h + \frac{1}{2} k_s h^2 - \pi w a^2 \\ &+ \mathcal{E} h^2 a + \frac{\pi}{2} \mathcal{E} f'(0) h a^2 + \mathcal{E} \frac{\pi^2}{12} f'(0)^2 a^3 + O(\|(a, h)\|^4). \end{aligned} \quad (\text{A.5})$$

563 When  $(a, h) = (0, 0)$  the value of  $\Pi(\cdot, \cdot; \Delta)$  equals  $k_s \Delta^2/2$ . Taking this into  
 564 account, it follows from (A.5) that in the limit  $(a, h) \rightarrow (0, 0)$  with  $a > 0$ ,

$$\Pi(a, h; \Delta) - \Pi(0, 0; \Delta) = -k_s \Delta h + \frac{1}{2} k_s h^2 - \pi w a^2 + O(\|(a, h)\|^3). \quad (\text{A.6})$$

565 First consider the case  $|\Delta| \neq 0$ . In this case, using (A.6), we can express  
 566 that

$$\Pi(a, h; \Delta) - \Pi(0, 0; \Delta) = -k_s \Delta h + O(\|(a, h)\|^2) \quad (\text{A.7})$$

567 in the limit  $(a, h) \rightarrow (0, 0)$  with  $a > 0$ . The asymptotic expansion given by (A.7)  
 568 holds for all sequences  $(a_n, h_n)_{n \in \mathbb{N}}$  converging to  $(0, 0)$  in which  $a_n > 0$ . An  
 569 example of such a sequence is  $(|\Delta|/n, \Delta/n)_{n \in \mathbb{N}}$ . In this sequence, it follows  
 570 from (A.7) and the definition of  $O(\cdot)$  that there exists an  $N \in \mathbb{N}$  such that for  
 571 all  $n > N$  the sign of  $\Pi(a_n, h_n; \Delta) - \Pi(0, 0; \Delta)$  is the same as that of  $-k_s \Delta^2/n$ .  
 572 Since  $k_s > 0$ , this result implies that no matter how small we choose  $\delta$  there  
 573 will always exist a point in  $B(0, 0, \delta)$  where the value of  $\Pi(\cdot, \cdot; \Delta)$  is smaller than

574 its value at the point  $(a, h) = (0, 0)$ . This proves that when  $|\Delta| \neq 0$ , the point  
 575  $(a, h) = (0, 0)$  cannot be a solution.

576 Now let us consider the case  $|\Delta| = 0$ . For this case, using (A.6), we can  
 577 express

$$\Pi(a, h; \Delta) - \Pi(0, 0; \Delta) = \frac{1}{2}k_s h^2 - \pi w a^2 + O(\|(a, h)\|^3). \quad (\text{A.8})$$

578 Consider the sequence  $(a_n, h_n)_{n \in \mathbb{N}}$  when  $a_n = |\Delta|/n$  and  $h_n = 0$ . Note that this  
 579 is an admissible sequence since  $a_n > 0$  for all  $n$ . For this sequence, it follows  
 580 from (A.8) and the definition of  $O(\cdot)$  that there exists an  $N \in \mathbb{N}$  such that for all  
 581  $n > N$  the sign of  $\Pi(a_n, h_n; \Delta) - \Pi(0, 0; \Delta)$  is the same as that of  $-\pi w \Delta^2/n^2$ .  
 582 Since  $w > 0$ , this result implies that no matter how small we choose  $\delta$  there will  
 583 always exist a point in  $B(0, 0, \delta)$  where the value of  $\Pi(\cdot, \cdot; \Delta)$  is smaller than its  
 584 value at the point  $(a, h) = (0, 0)$ . Hence, even in the case  $|\Delta| = 0$ , the point  
 585  $(a, h) = (0, 0)$  cannot be a solution.

## 586 Appendix B. Sign of $\chi(a; h)$

587 We take the negative root of  $\chi(a^\circ; h^\circ)$  from (2.15b). This is because a neg-  
 588 ative sign implies tensile tractions close to the contact periphery, whereas a  
 589 positive sign implies a compressive tractions close to the contact periphery. Ad-  
 590hesion indicates an attractive interaction between the surfaces. Thus, for the  
 591 case of adhesive contact, the traction in a region close enough to the contact pe-  
 592riphery has to be tensile when in equilibrium. The proof is as follows. According  
 593 to [35], the surface traction of the elastic half-space is

$$\begin{aligned} t_z(r, z = 0; h) &= -\frac{\mathcal{E}}{2r} \frac{d}{dr} \int_r^a \frac{\chi(\tilde{a}; h) \tilde{a}}{\sqrt{\tilde{a}^2 - r^2}} d\tilde{a} \\ &= -\frac{\mathcal{E}}{2r} \frac{d}{dr} \left[ \chi(a; h) \sqrt{a^2 - r^2} - \int_r^a \chi'(\tilde{a}; h) \sqrt{\tilde{a}^2 - r^2} d\tilde{a} \right] \\ &= -\frac{\mathcal{E}}{2r} \left[ -\chi(a; h) \frac{r}{\sqrt{a^2 - r^2}} + r \int_r^a \chi'(\tilde{a}; h) \sqrt{\tilde{a}^2 - r^2} d\tilde{a} \right] \\ &= \frac{\mathcal{E}}{2} \left[ \frac{\chi(a; h)}{\sqrt{a^2 - r^2}} - \int_r^a \chi'(\tilde{a}; h) \sqrt{\tilde{a}^2 - r^2} d\tilde{a} \right], \end{aligned} \quad (\text{B.1})$$

594 where  $\chi'(a; h) = \partial\chi(\tilde{a}; h)/\partial\tilde{a}$ . Let  $a = a^\circ$ ,  $h = h^\circ$ , and  $r = (1 - \epsilon)a^\circ$ , where  
 595  $\epsilon \rightarrow 0^+$ . After substituting, (B.1) becomes

$$t_z((1 - \epsilon)a^\circ; h^\circ) = \frac{\mathcal{E}}{2a^\circ} \left[ \frac{\chi(a^\circ; h^\circ)}{\sqrt{2\epsilon}} + O(\sqrt{\epsilon}) \right]. \quad (\text{B.2})$$

596 If the traction close to the contact periphery has to be negative (or tensile  
 597 traction according to the convention of [35]), then it requires that  $\chi(a^\circ; h^\circ) < 0$ ,  
 598 i.e.,

$$\chi(a^\circ; h^\circ) = -\sqrt{\frac{8a^\circ w}{\pi \mathcal{E}}}. \quad (\text{B.3})$$

599 Another reason why  $\chi(a^\circ; h^\circ) < 0$  is that the surfaces should not intersect  
600 with each other outside of the contact region. The displacement discontinuity  
601 outside the contact region  $[\tilde{u}]_z$  is [14]

$$[\tilde{u}_z(r; h)] = - \int_a^r \frac{\chi(\tilde{a}; h)}{\sqrt{r^2 - \tilde{a}^2}} d\tilde{a}. \quad (\text{B.4})$$

602 Let  $a = a^\circ$ ,  $h = h^\circ$ , and  $r = (1 + \epsilon)a^\circ$ , as  $\epsilon \rightarrow 0^+$ . Then, (B.4) becomes

$$\begin{aligned} [\tilde{u}_z((1 + \epsilon)a^\circ; h^\circ)] &= - \int_{a^\circ}^{(1+\epsilon)a^\circ} \frac{\chi(\tilde{a}; h^\circ)}{\sqrt{((1 + \epsilon)a^\circ)^2 - \tilde{a}^2}} d\tilde{a} \\ &= -\chi(a^\circ; h^\circ)\sqrt{2\epsilon} + O(\epsilon). \end{aligned} \quad (\text{B.5})$$

603 Because the surfaces do not intersect, this implies that  $[\tilde{u}]_z > 0$  outside the  
604 contact region. Therefore it requires that  $\chi(a^\circ; h^\circ) < 0$ .

### 605 Appendix C. Second order necessary and sufficient conditions on in- 606 terior solution points

607 In [Appendix C.1](#) we present the general form of the second order necessary  
608 condition on an interior solution point  $(a^*, h^*)$ , and a second order sufficient  
609 condition that a stationary point  $(a^\circ, h^\circ)$  needs to satisfy in order for it to be  
610 an interior solution point. Recall that a stationary point  $(a^\circ, h^\circ)$  is an interior  
611 point that is also a root of the function (2.20). These conditions are given in  
612 terms of the second partial derivatives of  $\Pi(\cdot, \cdot; \Delta)$ . We derive expressions for  
613 the second partial derivatives of  $\Pi(\cdot, \cdot; \Delta)$  at a stationary point in [Appendix C.2](#).  
614 In [Appendix C.3](#) we make use of those expressions to particularize and simplify  
615 the general conditions that we present in [Appendix C.1](#). In this section we take  
616  $(a^*, h^*)$  to denote an interior solution point.

#### 617 Appendix C.1. General second order necessary and sufficient conditions from 618 optimization theory

619 It can be shown that  $\Pi(\cdot, \cdot; \Delta)$  is twice continuously differentiable on  $\text{int}(\mathcal{D})$ .  
620 Therefore, it follows from standard nonlinear optimization theory that a sec-  
621 ond order necessary condition on  $(a^*, h^*)$  is that the value of its corresponding  
622 quadratic form is always non-negative. The quadratic form corresponding to a  
623 point  $(a, h)$  is the function  $Q(\cdot, \cdot; a, h) : \mathbb{R}^2 \setminus (0, 0) \rightarrow \mathbb{R}$ , where

$$Q(x, y; a, h) := x^2 \frac{\partial^2 \Pi}{\partial a^2}(a, h; \Delta) + 2xy \frac{\partial^2 \Pi}{\partial a \partial h}(a, h; \Delta) + y^2 \frac{\partial^2 \Pi}{\partial h^2}(a, h; \Delta). \quad (\text{C.1})$$

624 The quadratic form  $Q(\cdot, \cdot; a^*, h^*)$  is always non-negative iff

$$\frac{\partial^2 \Pi}{\partial h^2}(a^*, h^*; \Delta) \geq 0, \quad (\text{C.2a})$$

$$\frac{\partial^2 \Pi}{\partial a^2}(a^*, h^*; \Delta) \frac{\partial^2 \Pi}{\partial h^2}(a^*, h^*; \Delta) - \frac{\partial^2 \Pi}{\partial a \partial h}(a^*, h^*; \Delta)^2 \geq 0, \quad (\text{C.2b})$$

$$\frac{\partial^2 \Pi}{\partial a^2}(a^*, h^*; \Delta) \geq 0. \quad (\text{C.2c})$$

625 According to optimization theory, a sufficient condition for a stationary point  
626  $(a^\circ, h^\circ)$  to be an interior solution point is that the value of its corresponding  
627 quadratic form must always be positive. The quadratic form corresponding to  
628  $(a^\circ, h^\circ)$ , namely  $Q(\cdot, \cdot; a^\circ, h^\circ)$ , is always positive iff

$$\frac{\partial^2 \Pi}{\partial a^2}(a^\circ, h^\circ; \Delta) \frac{\partial^2 \Pi}{\partial h^2}(a^\circ, h^\circ; \Delta) - \frac{\partial^2 \Pi}{\partial a \partial h}(a^\circ, h^\circ; \Delta)^2 > 0, \quad (\text{C.3a})$$

$$\frac{\partial^2 \Pi}{\partial a^2}(a^\circ, h^\circ; \Delta) > 0. \quad (\text{C.3b})$$

629 *Appendix C.2. Second order partial derivatives of  $\Pi(\cdot, \cdot; \Delta)$  at an interior solu-*  
630 *tion point*

631 After differentiating (2.16) with respect to  $a$  and  $h$ , we find that

$$\frac{\partial^2 \Pi}{\partial a^2}(a, h; \Delta) = \frac{\pi^2 \mathcal{E}}{2} \chi(a; h) \frac{\partial \chi(a; h)}{\partial a} - 2\pi w, \quad (\text{C.4a})$$

$$\frac{\partial^2 \Pi}{\partial a \partial h}(a, h; \Delta) = \frac{\pi^2 \mathcal{E}}{2} \chi(a; h) \frac{\partial \chi(a; h)}{\partial h}, \quad (\text{C.4b})$$

$$\frac{\partial^2 \Pi}{\partial h^2}(a, h; \Delta) = \frac{\pi^2 \mathcal{E}}{2} \int_0^a \left\{ \left( \frac{\partial \chi(\tilde{a}; h)}{\partial h} \right)^2 + \chi(\tilde{a}; h) \frac{\partial^2 \chi(\tilde{a}; h)}{\partial h^2} \right\} d\tilde{a} + k_s. \quad (\text{C.4c})$$

632 It follows from (2.11) that

$$\frac{\partial \chi(\tilde{a}; h)}{\partial h} = \frac{2}{\pi}. \quad (\text{C.5})$$

633 In light of (C.5), (C.4) is reduced to

$$\frac{\partial^2 \Pi}{\partial a^2}(a, h; \Delta) = \frac{\pi^2 \mathcal{E}}{2} \chi(a; h) \frac{\partial \chi(a; h)}{\partial a} - 2\pi w, \quad (\text{C.6a})$$

$$\frac{\partial^2 \Pi}{\partial a \partial h}(a, h; \Delta) = \pi \mathcal{E} \chi(a; h), \quad (\text{C.6b})$$

$$\frac{\partial^2 \Pi}{\partial h^2}(a, h; \Delta) = 2\mathcal{E}a + k_s. \quad (\text{C.6c})$$

634 Equation (C.6) gives the second partial derivatives of  $\Pi(\cdot, \cdot; \Delta)$  at any interior  
635 point  $(a, h)$ . Using (C.6) we next evaluate the second partial derivatives of  
636  $\Pi(\cdot, \cdot; \Delta)$  at a stationary point  $(a^\circ, h^\circ)$ . To simply these derivatives, we first  
637 recall an important result discussed in §2.3.1, which is that

$$\chi(a^\circ; h^\circ) = -\sqrt{\frac{8a^\circ w}{\pi \mathcal{E}}}. \quad (\text{C.7})$$

638 We first substitute  $(a, h)$  in (C.6) with  $(a^\circ, h^\circ)$ . In the resulting equation, we  
639 then substitute  $\chi(a^\circ; h^\circ)$  with the expression on the right side of (C.7). After

640 simplifying, we determine that

$$\frac{\partial^2 \Pi}{\partial a^2}(a^\circ, h^\circ; \Delta) = -\sqrt{2\pi^3 a^\circ \mathcal{E} w} \frac{\partial \chi(a; h)}{\partial a} \Big|_{(a^\circ, h^\circ)} - 2\pi w, \quad (\text{C.8a})$$

$$\frac{\partial^2 \Pi}{\partial a \partial h}(a^\circ, h^\circ; \Delta) = -\sqrt{8\pi a^\circ \mathcal{E} w}, \quad (\text{C.8b})$$

$$\frac{\partial^2 \Pi}{\partial h^2}(a^\circ, h^\circ; \Delta) = 2\mathcal{E} a^\circ + k_s. \quad (\text{C.8c})$$

641 Recall that by definition  $(a^\circ, h^\circ)$  is a root of the function (2.20). The application  
 642 of the *Implicit function theorem* to function (2.20) infers the existence of the  
 643 function  $\mathfrak{h}$ , which is defined in (2.21). Additionally, it implies that

$$\frac{\partial \chi(a; h)}{\partial a} \Big|_{(a^\circ, h^\circ)} = -\sqrt{\frac{2w}{\pi a^\circ \mathcal{E}}} - \frac{2}{\pi} \mathfrak{h}'(a^\circ). \quad (\text{C.9})$$

644 We can then simplify (C.8a) to

$$\frac{\partial^2 \Pi}{\partial a^2}(a^\circ, h^\circ; \Delta) = \mathfrak{h}'(a^\circ) \sqrt{8\pi a^\circ \mathcal{E} w}. \quad (\text{C.10})$$

645 In summary, the second partial derivatives of  $\Pi(\cdot, \cdot; \Delta)$  at an interior solution  
 646 point are

$$\frac{\partial^2 \Pi}{\partial a^2}(a^\circ, h^\circ; \Delta) = \mathfrak{h}'(a^\circ) \sqrt{8\pi a^\circ \mathcal{E} w}, \quad (\text{C.11a})$$

$$\frac{\partial^2 \Pi}{\partial a \partial h}(a^\circ, h^\circ; \Delta) = -\sqrt{8\pi a^\circ \mathcal{E} w}, \quad (\text{C.11b})$$

$$\frac{\partial^2 \Pi}{\partial h^2}(a^\circ, h^\circ; \Delta) = 2a^\circ \mathcal{E} + k_s. \quad (\text{C.11c})$$

647 *Appendix C.3. Simplified second order necessary and sufficient conditions*

648 *Appendix C.3.1. A second order sufficiency condition for stationary points*

649 It follows from (C.11c) that  $\partial^2 \Pi / \partial h^2(a^\circ, h^\circ; \Delta) > 0$  at all stationary points,  
 650 since at any stationary point  $a^\circ > 0$  and by construction  $\mathcal{E}$  and  $k_s$  are positive.  
 651 Therefore, if  $(a^\circ, h^\circ)$  satisfies the inequality (C.3a), then it also satisfies the  
 652 inequality (C.3b). Therefore, in order for a point to be a solution point, the  
 653 only non-redundant sufficient condition on  $(a^\circ, h^\circ)$  is given by (C.3a). It follows  
 654 from (C.11) that a stationary point  $(a^\circ, h^\circ)$  satisfies the sufficient condition  
 655 (C.3a) iff

$$g(a^\circ) = \mathfrak{h}'(a^\circ) - \frac{\sqrt{8\pi a^\circ \mathcal{E} w}}{2a^\circ \mathcal{E} + k_s} > 0. \quad (\text{C.12})$$

656 *Appendix C.3.2. A second order necessary condition for interior solution points*

657 Since an interior solution point is also a stationary point (§2.3.1), then we  
658 obtain from (C.11) that

$$\frac{\partial^2 \Pi}{\partial a^2}(a^*, h^*; \Delta) = h'(a^*) \sqrt{8\pi a^* \mathcal{E} w}, \quad (\text{C.13a})$$

$$\frac{\partial^2 \Pi}{\partial a \partial h}(a^*, h^*; \Delta) = -\sqrt{8\pi a^* \mathcal{E} w}, \quad (\text{C.13b})$$

$$\frac{\partial^2 \Pi}{\partial h^2}(a^*, h^*; \Delta) = 2a^* \mathcal{E} + k_s. \quad (\text{C.13c})$$

659 The necessary condition (C.2a) does not lead to any additional conditions  
660 on the interior solution point  $(a^*, h^*)$ . This is because it follows from (C.13c)  
661 that at any interior solution point  $\partial^2 \Pi / \partial h^2(a^*, h^*; \Delta) > 0$ , since at any interior  
662 solution point  $a^* > 0$  and by construction  $\mathcal{E}$  and  $k_s$  are positive.

663 It follows from (C.13) that the necessary condition (C.2b) holds iff  $g(a^*) \geq 0$ .  
664 The function  $g$  is defined in (2.22). If  $(a^*, h^*)$  satisfies the necessary condition  
665 (C.2b), then it also satisfies the necessary condition (C.2c). This is because if  
666  $h'(a^*)$  is non-negative, then (C.13a) would imply that the necessary condition  
667 (C.2c) is satisfied.

668 If  $(a^*, h^*)$  satisfies the necessary condition (C.2b), then

$$g(a^*) = h'(a^*) - \frac{\sqrt{8\pi a^* \mathcal{E} w}}{2a^* \mathcal{E} + k_s}$$

669 is non-negative and

$$h'(a^*) \geq \frac{\sqrt{8\pi a^* \mathcal{E} w}}{2a^* \mathcal{E} + k_s}. \quad (\text{C.14})$$

670 At any interior solution point,  $a^*$  is positive. By construction,  $\mathcal{E}$  and  $k_s$  are  
671 positive and  $w$  is non-negative, thus (C.14) implies that  $h'(a^*)$  is non-negative.

## 672 **Appendix D. Fitting contact experimental data to theory**

673 In §4 we apply our model given in §3.1.1 to the experiments of Sun *et al.* [21]  
674 and Notbohm *et al.* [22]. It follows from (3.4b) and (3.5b) that the measured  
675 indentation depth,  $h$ , and the contact force,  $P$ , in those experiments should  
676 satisfy

$$h = F(P; \hat{a}, \hat{P}), \quad (\text{D.1})$$

677 where

$$F(P; \hat{a}, \hat{P}) := \frac{4^{2/3} \hat{a}^2}{R} \left[ \left( \frac{1 + \sqrt{1 + P/\hat{P}}}{2} \right)^{4/3} - \frac{2}{3} \left( \frac{1 + \sqrt{1 + P/\hat{P}}}{2} \right)^{1/3} \right],$$

678 and

$$\hat{a} := (9\pi w R^2 / 8\mathcal{E})^{1/3}, \quad (\text{D.2a})$$

$$\hat{P} := 3\pi w R / 2. \quad (\text{D.2b})$$

679 Say  $(h_i, P_i)$ ,  $i = 1, 2, \dots, n$ , where  $n$  is a positive integer, is a sequence of  
680 indentation depth–contact force measurements. An estimate of the mismatch  
681 between the theory and experimental results can be

$$S(\hat{a}, \hat{P}) := \sum_{i=1}^n r_i(\hat{a}, \hat{P})^2, \quad (\text{D.3})$$

682 where

$$r_i(\hat{a}, \hat{P}) := h_i - F(P_i; \hat{a}, \hat{P}), \quad (\text{D.4})$$

683 and  $i = 1, 2, \dots, n$ . We take the best values for the parameters  $\hat{a}$  and  $\hat{P}$  to be  
684 those at which  $S$  attains its minimum. Denoting the best fit values of  $\hat{a}$  and  $\hat{P}$   
685 as  $\hat{a}^*$  and  $\hat{P}^*$ , respectively, a necessary condition that  $S$  attains its minimum at  
686  $(\hat{a}^*, \hat{P}^*)$  is that

$$\frac{\partial S}{\partial \hat{a}}(\hat{a}^*, \hat{P}^*) = 0, \quad (\text{D.5a})$$

$$\frac{\partial S}{\partial \hat{P}}(\hat{a}^*, \hat{P}^*) = 0. \quad (\text{D.5b})$$

687 We obtain  $\hat{a}^*$  and  $\hat{P}^*$  by numerically solving (D.5a)–(D.5b), which are a pair  
688 of coupled, nonlinear algebraic equations. The best fit values for  $w$  and  $\mathcal{E}$   
689 are then obtained by simultaneously solving (D.2a)–(D.2b) for  $w$  and  $\mathcal{E}$  after first  
690 replacing in them  $\hat{a}$  and  $\hat{P}$  with their respective best fit values and  $R$  with its  
691 experimentally reported value.

## 692 References

- 693 [1] KL Johnson, K Kendall, and AD Roberts. Surface energy and the contact of  
694 elastic solids. *Proceedings of the Royal Society of London A: Mathematical,*  
695 *Physical and Engineering Sciences*, 324(1558):301–313, 1971.
- 696 [2] Kevin Kendall. *Molecular adhesion and its applications: The sticky uni-*  
697 *verse*. Springer US, 2001.
- 698 [3] Jacob N Israelachvili. *Intermolecular and surface forces*. Academic press,  
699 2011.
- 700 [4] Thomas Eisner and Daniel J Aneshansley. Defense by foot adhesion in a  
701 beetle (*hemisphaerota cyanea*). *Proceedings of the National Academy of*  
702 *Sciences*, 97(12):6568–6573, 2000.

- 703 [5] Eduard Arzt, Stanislav Gorb, and Ralph Spolenak. From micro to nano  
704 contacts in biological attachment devices. *Proceedings of the National*  
705 *Academy of Sciences*, 100(19):10603–10606, 2003.
- 706 [6] Gerrit Huber, Stanislav N Gorb, Naoe Hosoda, Ralph Spolenak, and Ed-  
707 uard Arzt. Influence of surface roughness on gecko adhesion. *Acta Bioma-*  
708 *terialia*, 3(4):607–610, 2007.
- 709 [7] James MR Bullock and Walter Federle. Beetle adhesive hairs differ in  
710 stiffness and stickiness: In vivo adhesion measurements on individual setae.  
711 *Naturwissenschaften*, 98(5):381–387, 2011.
- 712 [8] Jonas O Wolff and Stanislav N Gorb. Surface roughness effects on attach-  
713 ment ability of the spider *philodromus dispar* (araneae, philodromidae).  
714 *Journal of Experimental Biology*, 215(1):179–184, 2012.
- 715 [9] Fabienne Frost, Stanislav N Gorb, and Jonas O Wolff. Adhesion and friction  
716 in hunting spiders: The effect of contact splitting on their attachment  
717 ability. *Zoologischer Anzeiger*, 273:231–239, 2018.
- 718 [10] Danelle M Tanner, Norman F Smith, Lloyd W Irwin, William P Eaton,  
719 Karen Sue Helgesen, J Joseph Clement, William M Miller, Samuel L Miller,  
720 Micheal T Dugger, Jeremy A Walraven, and Kenneth A Peterson. MEMS  
721 reliability: Infrastructure, test structures, experiments, and failure modes.  
722 Technical report, Sandia National Labs., Albuquerque, NM (US); Sandia  
723 National Labs., Livermore, CA (US), 2000.
- 724 [11] Klaus Friedrich. *Friction and wear of polymer composites*, volume 1. Else-  
725 vier, 2012.
- 726 [12] Ian Hutchings and Philip Shipway. *Tribology: Friction and wear of engi-*  
727 *neering materials*. Butterworth-Heinemann, 2017.
- 728 [13] Rupert Stevenson Bradley. The cohesive force between solid surfaces and  
729 the surface energy of solids. *The London, Edinburgh, and Dublin Philo-*  
730 *sophical Magazine and Journal of Science*, 13(86):853–862, 1932.
- 731 [14] D. Maugis. *Contact Adhesion and Rupture of Elastic Solids*. Solid State  
732 Sciences. Springer, 2000.
- 733 [15] K Kendall. The adhesion and surface energy of elastic solids. *Journal of*  
734 *Physics D: Applied Physics*, 4(8):1186, 1971.
- 735 [16] J Kim, KS Kim, and YH Kim. Mechanical effects in peel adhesion test.  
736 *Journal of Adhesion Science and Technology*, 3(1):175–187, 1989.
- 737 [17] Tal Cohen, Chon U Chan, and L Mahadevan. Competing failure modes in  
738 finite adhesive pads. *Soft Matter*, 14(10):1771–1779, 2018.
- 739 [18] JA Hinkley. A blister test for adhesion of polymer films to SiO<sub>2</sub>. *The*  
740 *Journal of Adhesion*, 16(2):115–125, 1983.

- 741 [19] Z Cao, P Wang, W Gao, L Tao, JW Suk, RS Ruoff, D Akinwande, R Huang,  
742 and KM Liechti. A blister test for interfacial adhesion of large-scale trans-  
743 ferred graphene. *Carbon*, 69:390–400, 2014.
- 744 [20] Haneesh Kesari, Joseph C Doll, Beth L Pruitt, Wei Cai, and Adrian J  
745 Lew. Role of surface roughness in hysteresis during adhesive elastic contact.  
746 *Philosophical Magazine Letters*, 90(12):891–902, 2010.
- 747 [21] Yujie Sun, Boris Akhremitchev, and Gilbert C Walker. Using the adhesive  
748 interaction between atomic force microscopy tips and polymer surfaces to  
749 measure the elastic modulus of compliant samples. *Langmuir*, 20(14):5837–  
750 5845, 2004.
- 751 [22] Jacob Notbohm, Benny Poon, and Guruswami Ravichandran. Analysis of  
752 nanoindentation of soft materials with an atomic force microscope. *Journal*  
753 *of Materials Research*, 27(1):229–237, 2012.
- 754 [23] Nicolas Bouchonville, Mikaël Meyer, Christophe Gaude, Emmanuel Gay,  
755 David Ratel, and Alice Nicolas. AFM mapping of the elastic proper-  
756 ties of brain tissue reveals kpa  $\mu\text{m}^{-1}$  gradients of rigidity. *Soft Matter*,  
757 12(29):6232–6239, 2016.
- 758 [24] Donna M Ebenstein and Kathryn J Wahl. A comparison of JKR-based  
759 methods to analyze quasi-static and dynamic indentation force curves.  
760 *Journal of Colloid and Interface Science*, 298(2):652–662, 2006.
- 761 [25] Dongchan Ahn and Kenneth R Shull. JKR studies of acrylic elastomer  
762 adhesion to glassy polymer substrates. *Macromolecules*, 29(12):4381–4390,  
763 1996.
- 764 [26] Donna M Ebenstein and Lisa A Pruitt. Nanoindentation of biological ma-  
765 terials. *Nano Today*, 1(3):26–33, 2006.
- 766 [27] Weilin Deng and Haneesh Kesari. Depth-dependent hysteresis in adhesive  
767 elastic contacts at large surface roughness. *Scientific Reports*, 9(1):1639,  
768 2019.
- 769 [28] Kunio Takahashi, Ryoji Mizuno, and Tadao Onzawa. Influence of the stiff-  
770 ness of the measurement system on the elastic adhesional contact. *Journal*  
771 *of Adhesion Science and Technology*, 9(11):1451–1464, 1995.
- 772 [29] Fuqian Yang. Load–displacement relation in adhesion measurement. *Jour-  
773 nal of Physics D: Applied Physics*, 36(19):2417, 2003.
- 774 [30] Haneesh Kesari and Adrian J Lew. Effective macroscopic adhesive contact  
775 behavior induced by small surface roughness. *Journal of the Mechanics and*  
776 *Physics of Solids*, 59(12):2488–2510, 2011.

- 777 [31] Ivan Argatov, Qiang Li, Roman Pohrt, and Valentin L Popov. Johnson–  
778 Kendall–Roberts adhesive contact for a toroidal indenter. *Proceedings of*  
779 *the Royal Society A: Mathematical, Physical and Engineering Sciences*,  
780 472(2191):20160218, 2016.
- 781 [32] Emanuel Willert, Qiang Li, and Valentin L Popov. The JKR-adhesive  
782 normal contact problem of axisymmetric rigid punches with a flat annular  
783 shape or concave profiles. *Facta Universitatis, Series: Mechanical Engi-*  
784 *neering*, 14(3):281–292, 2016.
- 785 [33] Valentin L Popov, Roman Pohrt, and Qiang Li. Strength of adhesive  
786 contacts: Influence of contact geometry and material gradients. *Friction*,  
787 5(3):308–325, 2017.
- 788 [34] Ian N Sneddon. The relation between load and penetration in the axisym-  
789 metric Boussinesq problem for a punch of arbitrary profile. *International*  
790 *Journal of Engineering Science*, 3(1):47–57, 1965.
- 791 [35] Haneesh Kesari and Adrian J Lew. Adhesive frictionless contact between  
792 an elastic isotropic half-space and a rigid axi-symmetric punch. *Journal of*  
793 *Elasticity*, 106(2):203–224, 2012.
- 794 [36] Weilin Deng and Haneesh Kesari. Molecular statics study of depth-  
795 dependent hysteresis in nano-scale adhesive elastic contacts. *Modelling and*  
796 *Simulation in Materials Science and Engineering*, 25(5):055002, 2017.